The Effect of Density Ratio on Steep Injection Angle Purge Jet Cooling for a Converging Nozzle Guide Vane Endwall at Transonic Conditions

Ridge Alexander Sibold

Thesis submitted to the faculty of the Virginia Polytechnic Institute and State University in partial fulfillment of the requirements for the degree of

Master of Science
In
Mechanical Engineering

Wing F. Ng, Chair
K. Todd Lowe
Thomas E. Diller
Hang Ruan

August 8, 2019
Blacksburg, VA

Keywords: Experimental Heat Transfer, Film Cooling, Endwall Heat Transfer,
Endwall Film Cooling, Density Ratio, Blowing Ratio, Purge Flow,
Secondary Flows, Transonic, Gas Turbines, Momentum Ratio

The Effect of Density Ratio on Steep Injection Angle Purge Jet Cooling for a Converging Nozzle Guide Vane Endwall at Transonic Conditions

Ridge Alexander Sibold

ABSTRACT

The study presented herein describes and analyzes a detailed experimental investigation of the effects of density ratio on endwall thermal performance at varying blowing rates for a typical nozzle guide vane platform purge jet cooling scheme. An axisymmetric converging endwall with an upstream doublet staggered cylindrical hole purge jet cooling scheme was employed. Nominal exit flow conditions were engine representative and as follows: $\mathrm{Ma}_{\mathrm{Exit}} = 0.85$, $\mathrm{Re}_{\mathrm{Exit},\mathrm{C}_{\mathrm{ax}}} = 1.5 \times 10^6$, and large-scale freestream Tu = 16%. Two blowing ratios were investigated corresponding to the upper and lower engine extrema. Each blowing ratio was investigated amid two density ratios; one representing typical experimental neglect of density ratio, at DR = 1.2, and another engine representative density ratio achieved by mixing foreign gases, DR = 1.95. All tests were conducted on a linear cascade in the Virginia Tech Transonic Blowdown Wind Tunnel using IR thermography and transient data reduction techniques. Oil paint flow visualization techniques were used to gather quantitative information regarding the alteration of endwall flow physics due two different blowing rates of high-density coolant. High resolution endwall adiabatic film cooling effectiveness, Nusselt number, and Net Heat Flux Reduction contour plots were used to analyze the thermal effects.

The effect of density is dependent on the coolant blowing rate and varies greatly from the high to low blowing condition. At the low blowing condition better near-hole film cooling performance and heat transfer reduction is facilitated with increasing density. However, high density coolant at low blowing rates isn’t adequately equipped to penetrate and suppress secondary flows, leaving the SS and PS largely exposed to high velocity and temperature mainstream gases. Conversely, it is observed that density ratio only marginally affects the high blowing condition, as the momentum effects become increasingly dominant. Overall it is concluded density ratio has a first order impact on the secondary flow alterations and subsequent heat transfer distributions that occur as a result of coolant injection and should be accounted for in purge jet cooling scheme design and analysis.

Additionally, the effect of increasing high density coolant blowing rate was analyzed. Oil paint flow visualization indicated that significant secondary flow suppression occurs as a result of increasing the blowing rate of high-density coolant. Endwall adiabatic film cooling effectiveness, Nusselt number, and NHFR comparisons confirm this. Low blowing rate coolant has a more favorable thermal impact in the upstream region of the passage, especially near injection. The low momentum of the coolant is eventually dominated and entrained by secondary flows, providing less effectiveness near PS, near SS, and into the throat of the passage. The high momentum present for the high blowing rate, high-density coolant suppresses these secondary flows and provides enhanced cooling in the throat and in high secondary flow regions. However, the increased turbulence impartation due to lift off has an adverse effect on the heat load in the upstream region of the passage. It is concluded that only marginal gains near the throat of the passage are observed with an increase in high density coolant blowing rate, but severe thermal penalty is observed near the passage onset.

The Effect of Density Ratio on Steep Injection Angle Purge Jet Cooling for a Converging Nozzle Guide Vane Endwall at Transonic Conditions

Ridge Alexander Sibold

GENERAL AUDIENCE ABSTRACT

Gas turbine technology is used frequently in the burning of natural gas for power production. Increases in engine efficiency are observed with increasing firing temperatures, however this leads to the potential of overheating in the stages following. To prevent failure or melting of components, cooler air is extracted from the upstream compressor section and used to cool these components through various highly complex cooling schemes. The design and operational adequacy of these schemes is highly subject to the mainstream and coolant flow conditions, which are hard to represent in a laboratory setting.

This experimental study explores the effects of various coolant conditions, and their respective response, for a purge jet cooling scheme commonly found in engine. This scheme utilizes two rows of staggered cylindrical holes to inject air into the mainstream from platform, upstream of the nozzle guide vane. It is the hope that this air forms a protective layer, effectively shielding the platform from the hostile mainstream conditions. Currently, little research has been done to quantify these effects of purge flow cooling scheme while mimicking engine geometry, mainstream and coolant conditions.

For this study, an endwall geometry like that found in engine with a purge jet cooling scheme is studied. Commonly, an upstream gap is formed between the combustor lining and first stage vane platform, which is accounted for in this testing. Mainstream and coolant flow conditions can have large impacts on the results gathered, so both were matched to engine conditions. Varying of coolant density and injection rate is studied and quantitative results are gathered. Results indicate coolant fluid density plays a large role in purge jet cooling, and with neglection of this, potential thermal failure points could be overlooked This is exacerbated with less coolant injection. Interestingly, increasing the amount of coolant injected decreases performance across much of the passage, with only marginal gains in regions of complex flow. These results help to better explain the impacts of experimental neglect of coolant density, and aid in the understanding of purge jet coolant injection.

ACKNOWLEDGEMENTS

First, I would like to acknowledge that the pursuit of this degree would not be possible without the immense blessings God has provided me. From the opportunity to attend Virginia Tech, to instilling the drive and determination to achieve all necessary, to the support system carefully placed around to uplift and strengthen me, God's unwavering hand of support and love has always been present. I am, and always have been, extremely blessed throughout this process, and for that, I am forever thankful.

I would like to express the upmost gratitude to my advisor and mentor, Dr. Wing Ng, who is responsible for guiding me throughout this journey. Dr. Ng took a chance inviting me into his research group, and it is my sincerest hope that I met and exceeded all expectations set forth from a personal and professional standpoint. Without the guidance, tutelage, and motivation given by Dr. Ng, the work presented herein would not have been achievable, and I would not be the matured engineer I am as a result. Dr. Ng's mentoring from a technical, communicative, and personal standpoint has molded and influenced every aspect of my life and aided in my transition from a student to a professional. Finally, I would like to thank Dr. Ng for allowing me to pursue a challenging research topic that piqued my interest.

I would like to extend many thanks to my committee members, Dr. Thomas Diller, Dr. Todd Lowe, and Dr. Hang Ruan, for their valuable mentorship and suggestions. Virginia Tech is filled with world-renowned faculty; however, I feel privileged to have had the distinct pleasure to work alongside those listed. Additionally, I sincerely thank them for their willingness to serve on my committee and offer helpful advice and counsel.

It has been to my advantage to work with two industry sponsors during my pursuit of a master's degree: Solar Turbines Inc. and NanoSonic Inc. It has been a great learning experience working with an industry contemporary such as Solar Turbines, specifically with sponsors as knowledgeable and helpful as Hongzhou Xu and Michael Fox. I would like to thank Solar Turbines, and all involved; for enabling me to research a challenging project that was relevant to today's research community. Additionally, a special thank you to Hang Ruan and Echo Kang, my industry project sponsors from NanoSonic Inc. Their leadership, guidance, and trust enabled me to participate in a multitude of additional research projects that helped to broaden my horizon both professionally and personally. This experience will be invaluable in my career moving forward. I would like to thank both companies mentioned for their funding in my pursuit of a master's degree.

The completion of this work would not have been possible without the brilliant support system surrounding me, comprised of my closet family, friends, and coworkers. Specifically, I want to thank my mother, Ginger Sibold-Baldwin, my father, Dewey Sibold, and my sister, Ragan Proffitt for their continuous support and love. The knowledge and determination my parents instilled at a young age played a large role in the earning of this degree. Additional to my parents, I would like to extend my deepest thanks towards my stepparents, Adam Baldwin and Lynne Hazelwood. Without their guidance and advice these works would not have been possible. Although each deserves to be mentioned, I would like to extend thanks to each and every member of my family that has not been mentioned. The outpouring of support and faith in me has not gone unnoticed and I thank each of you for this.

A special thanks goes out to all researchers at the Advanced Propulsion and Power Laboratory. The lab environment and friends made along the way made for a very friendly and inviting research setting. A special thanks goes out to Luke Luehr, Shuo Mao, Jaideep Pandit, Renzo Larosarivero, Vy Nguyen, Matt Bogdan, Andrew Boulanger, Albrey de Clerck and all other members of the Heat, Energy, and Fluids Transport Lab. It is only with their friendship and advice that I was able to achieve this goal. Also, thank you to all previous researchers on the Solar Turbines Research Project at Virginia Tech, as their research formed the foundation of the results presented herein. A special thank you goes out to all undergraduates who researched with the group during my tenure. Specifically, I extend my deepest thanks to Stephen Lash, Blaine Hugger, and Jin Woo Lee for their hard work and toleration of my perfectionist attitude and workaholic tendencies. Without their willingness to work alongside me for long hours, it is doubtful this would have been achieved. Finally, I would like to extend many thanks to the support staff at Virginia Tech, specifically Diana Israel, Randall Monk, and the entire ME machine shop, for without them this would not have been impossible.

Table of Contents

List of Figures

List of Tables

List of Equations

Nomenclature

A	Area
C	Vane Chord
CFD	Computational Fluid Dynamics
C_r	Recovery Coefficient
D	Diameter
DLRT	Dual Linear Regression Technique
DR	Density Ratio, $\frac{\rho_c}{\rho_\infty}$
HSV	Horseshoe Vortex
HTC	Heat transfer Coefficient, $W/_{m^2K}$
IR	Infrared
k	Thermal Conductivity, $W/_{mK}$
LE	Leading Edge
M	Blowing Ratio, $\frac{\rho_c V_c}{\rho_\infty V_\infty}$
Ma	Mach Number
MFR	Mass Flow Ratio, $\frac{\dot{m}_c}{\dot{m}_\infty}$
MR	Momentum Ratio, $\frac{\rho_c V_c^2}{\rho_\infty V_\infty^2}$
NHFR	Net Heat Flux Reduction
Nu	Nusselt Number
P	Pitch
p	Pressure
PS	Pressure Side
q”	Heat Flux
Re	Reynolds Number
SF_6	Sulfur Hexafluoride
SS	Suction Side
T	Temperature
TE	Trailing Edge

Tu	Turbulence Intensity
V	Velocity
VR	Velocity Ratio, $\frac{V_c}{V_\infty}$

Greek

α	Coolant Injection Angle
γ	Specific Heat Ratio
η	Adiabatic Film Cooling Effectiveness
ρ	Density
φ	Overall Film Effectiveness

Subscripts

ax	Axial
c	Coolant Flow
f	Film Cooled Case
HDR	High Density Ratio Case
HM	High Blowing Ratio Case
LDR	Low Density Ratio Case
LM	Low Blowing Ratio Case
r	Recovery
S	Static
T	Total
w	Wall
∞	Freestream Flow

Introduction

With the ever-growing need for cleaner and more efficient energy, the use of gas turbines has steadily increased since the early 1900's. Prior to the 1960's the aviation industry was the primary user of gas turbine technology. However, gas turbines are currently used for marine applications, aircraft propulsion, and generation of more than 50% of the world market for thermal power plants [1]. Thermodynamically, gas turbines follow the traditional Brayton Cycle which inherently increase efficiency with increasing turbine inlet temperatures. The need for more efficient power generation, coupled with the constraint of pollution mitigation, has led the industry toward more complex and advanced combustor designs. Recent combustor design changes have resulted in flattened combustor exit profiles and higher operational temperatures [2,3]. Consequently, heat transferred into the hot section components has increased beyond the thermal threshold of component materials, especially first stage nozzle guide vane (NGV) platforms due to their proximity to the combustor and the high levels of turbulence subjected. To mitigate thermal failure and achieve long term durability goals, thermal barrier coatings and sophisticated cooling techniques have been developed and implemented. Internal cooling, showerhead film cooling, discrete hole endwall film cooling, purge flow film cooling, trailing edge cooling, and mateface leakage cooling are only several of the common methods manufactures use to offset the malfunctions created by increasing thermal loads. In addition to attenuating the wall heat flux, literature has also shown that strategic positioning of coolant injection can suppress adverse secondary flows and aid in aerodynamic loss minimization.

Effectiveness of purge jet cooling schemes is highly dependent on freestream and secondary flow conditions at the point of injection, which can be difficult to replicate in many instances. During engine operation, secondary coolant fluid is pulled from the compressor section, routed around the combustion section, and injected. The coolant fluid is generally at significantly higher pressures and lower temperatures than the mainstream flow resulting in a density ratio between coolant and mainstream of near 2. Often matching coolant density is neglected in experimentation and similar fluids are used for the mainstream and coolant, resulting in a coolant to mainstream density ratio near or at 1. The endwall secondary flow, heat transfer, and film effectiveness alterations due to experimental neglect of realistic density ratios could lead to endwall hot spot generation, and ultimately thermal failure of critical components. The research herein examines the effect of neglecting density ratio in laboratory experimentation, as well as the effect of an engine representative purge jet cooling scheme with engine consistent mainstream conditions, coolant conditions, and geometry. This will further aid in the understanding, testing, and designing of hot section components.

Relevant Past Studies

Endwall aerodynamics has been a topic of heavy research dating back to before the 1970's. Some of the most influential works in the field include, but are not limited to, the following research documents. Sieverding [4] summarized all experimentation done prior to 1985 and concluded that a good understanding of the secondary flow patterns had been obtained, yet more was needed regarding the significance of each. Sharma and Butler [5] determined a semi-empirical method of estimating secondary flows and endwall losses for cascades using a thorough review of literature and pressure loss data. Influences of aspect ratio, position of traversing planes, and inlet side wall boundary layer were investigated using 5-hole probe methods, flow visualization, and static pressure measurements by Jilek [6]. It was determined that the position and size of the high loss region in-passage depends on the axial distance of the cascade, the profile shape, and the inlet boundary layer. Goldstien and Spores [7] utilized a naphthalene mass transfer technique to investigate the effects of freestream Reynolds number and endwall boundary layer thickness on the complex three-dimensional flow in-passage. It was found that the inlet conditions have a first-order effect on in-passage secondary flow. A model referenced in most gas turbine research presently was developed by Wang et al. [8] using smoke wires and an illuminating laser sheet. From these works, it is concluded that the stagnation of the incoming boundary at the leading edge forms a horseshoe vortex (HSV) due to the inherent velocity gradient present. The HSV then bifurcates into two vortex systems: one traveling downstream on the suction side (SS) and the other on the pressure side (PS). During migration downstream, both vortex systems collapse to form one dominant vortex on each side, the pressure side and suction side horseshoe vortices. The PS HSV is swept across passage, from pressure side to suction side, due to endwall pressure gradients and entrains the main flow and inlet boundary layer. The merger of the SS and PS horseshoe vortices create an intense counter rotating vortex known as the passage vortex. The maturation in size and intensity of the passage vortex creates an additional smaller counter rotating vortex which Wang et al. [8] first called the wall vortex.

Additional to the endwall flow physics that exist in a turbine passage, much research and investigation has been done in the field of endwall heat transfer. Graziani et al. [9] used a large-scale, low-speed wind tunnel to investigate the effects of boundary layer thickness on endwall heat transfer. It was determined that the inlet boundary layer has a first order effect on secondary flows and heat transfer in the passage. Boyle and Hoose [10] showed that the dominant features prevalent in a flat endwall cascade, excluding the leading edge region, are reproducible using a curved duct. An in-depth investigation of endwall flow physics was completed by Kang and Thole [11] using Laser Doppler Velocimetry (LDV) and compared to previously reported heat transfer data. The comparison yielded results showing that high heat transfer regions were formed where the mainstream fluid was forced back toward the endwall surface in the downward leg of the vortices. Additionally, it was found that a dip in heat transfer occurred where the passage vortex lifted from the endwall. Boyle and Russell [12] used a combination of experimental techniques including the use of liquid crystal, foil heaters, static pressure taps, and a three-hole probe to accurately gather heat transfer and secondary flow data for a range of inlet conditions. It was determined that the heat transfer distribution on the endwall of a turbine stator is directly related to the secondary flows in the cascade, which are significantly altered for various inlet flow conditions.

With regards to inlet conditions, much research has been conducted investigating how endwall heat transfer is altered under various mainstream conditions. First stage nozzle guide vane platforms can be subjected to high levels of turbulence from the flow exiting the combustor. Turbulence effects were investigated in low-speed tunnels using constant heat flux boundary conditions by Ames et al. [13], using narrow band thermochromic liquid crystal thermometry, and Radomsky and Thole [14], using infrared (IR) thermography. It was concluded from both studies that increasing turbulence augmented heat transfer on the endwall, but this effect was less prevalent in high secondary flow regions such as near the leading edge (intense secondary flows due to horseshoe vortex system formation) and near suction side (intense secondary flows due to passage vortex). Schmidt and Bogard [15] extended the study of high turbulence levels with large length scales to a film cooled flat plate using IR thermography. At low coolant momentum, attachment was facilitated following the hole and was adversely affected by the increased turbulence levels. Conversely, whenever coolant momentum increased to a sufficient level to cause jet lift-off, the trend was reversed, and film cooling effectiveness was increased with increased turbulence due to greater jet dispersion. Laveau et al. [16] investigated the effects of increasing the Reynolds and

Mach numbers simultaneously by increasing the mass flow through the test section while utilizing embedded PT100 Sensors, IR thermography, and computational fluid dynamics (CFD) for data gathering and analysis. The increase in mass flow led to an associated augmentation of endwall heat transfer. These results are further investigated by Spencer et al. [17], in which a transient liquid crystal technique was employed to independently investigate the effect of Reynolds and Mach number, and Hippensteele and Russell [18], who investigated the effect of freestream Reynolds number using liquid crystal techniques. Results show that an increase in either freestream Mach or Reynolds number results in significant endwall secondary flow alteration and augmented heat transfer, particularly near leading edge, pressure side trailing edge, and suction side. The essentiality of matching mainstream flow conditions is illustrated due to endwall secondary flow and heat transfer dependence.

The effects of upstream and endwall geometry has been shown to have influence on endwall secondary flows and heat transfer distributions. Changes in upstream geometry were studied by De la Rose Blanco et al. [19], Colban et al. [20,21], and Piggush and Simon [22] in low-speed linear cascades. It was determined by each that the upstream geometry had a significant impact on altering the intensity and distribution of in-passage secondary flows and heat transfer. More recently, Mayo et al. [23] and Li et al. [24] used a transonic blowdown facility and numerical techniques respectively to study the effects of an upstream gap and misalignment, created by the combustor/vane interface, at transonic conditions. It was found that a small cavity vortex was formed in the gap, which grew in size and intensity with larger backward-facing steps (combustor lining above NGV platform). A forward-facing step in the presence of this gap diminished the cavity vortex almost entirely. Gustafson et al. [25] used a low speed experiment to illustrate a non-axisymmetric contoured endwall shifting the horseshoe vortex upstream, reducing cross flow and the size of the passage vortex, and minimizing passage vortex lift-off. Panchal et al. [26] reiterated the secondary flow shifting due to non-axisymmetric contouring by illustrating a decrease in endwall heat transfer magnitude, especially in typical high secondary flow regions. More pertinent to this study is axisymmetric endwall contouring. Thrift et al. [27,28] used foil heaters and IR thermography, Shih et al. [29] used CFD, Dossena et al. [30] used a miniature 5-hole probe and CFD, and Okita and Nakamata [31] used only CFD to collectively study the heat transfer and aerodynamic effects associated with an axisymmetric endwall as compared to a planar endwall. Overall, it is concluded that the axisymmetric contouring of the endwall accelerates the flow creating a favorable pressure gradient and thinning the boundary layer which weakens cross-stream pressure gradients and endwall secondary flows. Heat transfer and film effectiveness levels for upstream cooling were improved in the presence of axisymmetric endwall contouring for all cases. Collectively, results indicate engine representative geometry should be employed to accurately mimic and understand the secondary flows and heat transfer distributions found in engine.

In recent years, much research has been done on the various types of film cooling technology and is documented in Dunn [32], Chyu [33], Simon and Piggush [34], Bogard and Thole [35], and Bunker [36]. It is outside the scope of the present study to consider all platform cooling techniques; therefore, only purge flow cooling schemes are considered. Lynch and Thole [37], Saxena et al. [38], and Roy et al. [39] investigated the effects of slot geometry and flow rate at low-speeds and transonic conditions for various endwall geometries. It was observed that low momentum coolant from the slot often led to domination by the endwall secondary flows. Conversely, if coolant momentum was increased beyond a critical point, increased mixing occurred and lowered the film effectiveness even for increasing coolant mass flow rates. In general, the leakage of coolant from the upstream purge slot had a positive effect on the thermal load on the near slot portion of the endwall, even amid augmented heat transfer coefficient (HTC) levels.

Less commonly, purge flow is injected through discrete holes rather than a slot. For differentiation, this is referred to as purge jet cooling. The cooling jets greatly differ in flow physics, heat transfer impact, and film effectiveness as compared to upstream purge slot cooling, requiring separate analysis. Purge jet cooling is directly applicable to the research presented herein, but less documented in literature. Oke et al. [40] researched the effect of a contoured endwall on a bleed flow that is similar to a purge jet cooling scheme. It was shown that discrete hole injection was 20-30% less effective near-hole due to increased mixing. However, increasing the bleed flow rate had significant impacts on far passage cooling, particularly near PS. Pressure sensitive paint techniques were employed to compare a doublet staggered hole purge jet cooling scheme to a single discrete slot cooling scheme on a flat endwall at transonic mainstream conditions by Zhang and Jaiswal [41]. It was observed that both cooling schemes suffered from secondary flow domination at low coolant mass flow rates, but with increasing coolant mass flow it was evident that the slot provided a more uniform distribution near injection, while the doublet staggered purge jet cooling scheme penetrated further into the passage. Zhang and Moon [42,43] used a similar technique and mainstream conditions in two studies to jointly investigate the effect of a backward-facing step on a purge jet cooling scheme at an injection angle of 30°, and the feasibility of increasing coolant velocity to offset identified negative effects associated with said step. Jointly, it was concluded that a backward facing step enhanced secondary flow formation and strength, resulting in poor film performance at low coolant mass flow rates. As the coolant to mainstream mass flow ratio (MFR) increased, and subsequent coolant velocity, the coolant suppressed the secondary flows and significant gains in coolant effectiveness were observed, particularly toward the pressure side trailing edge. In a study with similar mainstream conditions, endwall geometry, and coolant geometry to the research presented herein, El-Gabry et al. [44] used pressure sensitive paint (PSP) techniques and CFD to analyze the effect of injection angle and coolant mass flow rate on a purge jet cooling scheme. Results show that increasing the injection angle generally decreases the effectiveness, while increasing the mass flow ratio increases the effectiveness and penetration into the passage. High mass flow ratio coolant tends to lift from the endwall, especially with increasing injection angles, leading to uncooled regions just downstream of injection location. None of the afore mentioned studies present heat transfer data, leaving a void in the complete analysis. Additionally, all studies presented use a density ratio of near or at unity, which is far from density ratios typical in gas turbine engines (≈ 2.0).

Heat transfer and film effectiveness alterations due to the injection of cooling fluid with various density on flat plates has been largely researched by Pederson et al. [45], Baldauf et al. [46,47], and Johnson et al. [48], amongst others, using mass transfer analogy, IR thermography, and pressure sensitive paint and particle image velocimetry techniques respectively. Results show that near-hole heat transfer and film cooling effectiveness was affected by coolant density to a first order degree. Generally, increasing coolant fluid density led to a more favorable momentum ratio, thus aiding in coolant attachment, lowering the heat transfer and increasing film effectiveness near-hole. Coolant progression far downstream was not discussed in these studies. Nazary et al. [49] extended the investigation of coolant density to an upstream slot and endwall discrete-hole cooling configuration for a flat endwall. The temperature sensitive paint (TSP) technique was used and foreign gases, $\mathrm{CO_2}$ (Carbon Dioxide) and $\mathrm{SF_6}$ (Sulfur Hexafluoride) were utilized to model the higher density coolant. Increased coolant density proved detrimental to the cooling effectiveness for the upstream slot due to the decreasing of an already minimal coolant momentum, conversely it was observed that the in-passage discrete hole cooling benefited. Two recent studies most relevant to the investigation reported herein are Chen et al. [50] and Li et al. [51], both of whom investigated the effects of coolant density for a single upstream row of discrete holes on a three-dimensionally contoured and flat endwall respectively. Both tests were low-speed and utilized a combination of pressure sensitive paint (PSP) and numerical techniques to illustrate the effects of varying coolant to mainstream density ratio. High density coolant provided high near-hole effectiveness but degraded quickly due to dominating secondary flows, leaving the PS largely uncooled. Conversely, low density coolant provided low cooling effectiveness levels following the holes, due to increased coolant momentum resulting in lift-off. Following reattachment, the high coolant momentum suppressed in-passage secondary flows and pressure gradients, allowing coolant penetration further into the passage. Interestingly, the three studies involving engine representative geometries employed pressure or temperature sensitive paint techniques at low speeds. These experiments provided no heat transfer data, and engine representative mainstream conditions were not matched.

Research Motivation and Objective

The literature study prior provides valuable insight into many mechanisms that pertain to endwall heat transfer and purge jet cooling scheme effectiveness. Conclusions from literature show that endwall geometry, cooling geometry, and mainstream and coolant flow conditions impact film cooling effectiveness and endwall heat transfer to a first order degree. Presently, no research has demonstrated the effects of an upstream purge jet flow in the presence of engine representative geometry while matching mainstream and coolant flow conditions. Furthermore, the small amount of work investigating coolant density for a purge jet cooling scheme at low speeds lacks heat transfer data. Any illustration of the effect of coolant density on purge jet cooling at engine matched conditions and geometry while reporting heat transfer and film cooling data would be the first in open literature.

The present study investigates the effect of density ratio on a doublet staggered purge jet cooling scheme. An axisymmetric converging endwall is employed that mimics an engine representative inner endwall. Engine representative Reynolds number, Mach number, and turbulence intensities are used for the mainstream flow, and the blowing rates tested are consistent with the upper and lower spectra of those found in engine. Finally, the density ratio between coolant and mainstream is varied between near unity (1.2), commonly the case in open literature when coolant density is neglected, and 1.95, representative of engine conditions. The results reported should lead to improvements in purge jet cooling understanding and testing.

Experimental Methodology

A. Virginia Tech Transonic Blowdown Wind Tunnel

The facility utilized for the experimental results presented was the Virginia Tech Transonic Blowdown Wind Tunnel located at the Advanced Propulsion and Power Laboratory at the Virginia Tech Corporate Research Center. The facility is a blowdown type tunnel where quasi-steady aerodynamic and transient heat transfer experiments are conducted on linear cascades. The tunnel has a maximum mass flow rate of 4.5 kg/s and is capable of 30 second test runs at exit Mach numbers between 0.6 and 1.2. A 5000 gallon air tank is pressurized by two Boge Industrial Air Compressors, capable of 1.27 kg/s mass flow rates at pressures of 1207 kPa, prior to the test run and discharged as the mainstream flow. To ensure minimal moisture content, air is directed through an Aircell dryer before entering the tank effectively lowering the dew point to near -70℃. The mainstream flow is controlled by two pneumatically actuated valves before entering the tunnel. The first is a safety valve which prevents over pressurization. The second is a butterfly control valve that regulates flow according to an in-house developed algorithm to ensure steady inlet pressures during the data recording window. The program progressively actuates the valve according to predefined sequences to counteract the pressure drop associated with draining the storage tank.

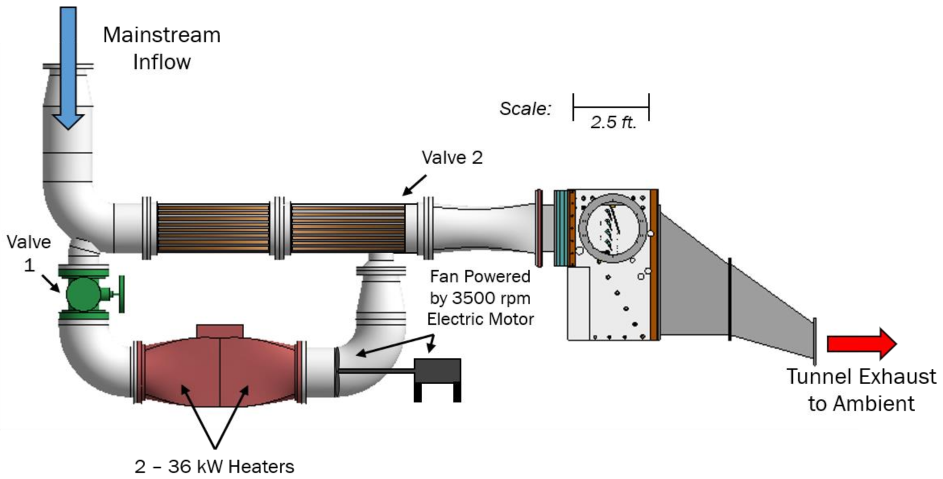

Figure 1. Virginia Tech Transonic Wind Tunnel Facility

For heat transfer experiments, a copper pipe heat exchanger is heated by two 36 kW heaters. During this process Valve 1 is opened and Valve 2 closed, effectively allowing a fan to circulate air, creating a forced convection loop but restricting flow to the test section so that no endwall pre-heating occurs. In the top portion of the heating loop, the air passes through several hundred copper pipes that not only act as flow straighteners during blowdown, but also hold the heat transferred from the recirculating flow. The air temperature, heater temperature, and copper tubing temperature are monitored via thermocouple measurements. Heating is continued until the air reaches the desired temperature at which point Valve 1 is closed and Valve 2 opened. Directly following valve actuation, the control sequence for the safety and control valve begins, starting a 30 second blowdown with transient mainstream temperature. An important consideration to note is that although the mainstream air is heated, no effort is made toward matching mainstream engine flow temperatures. The tunnel is modular in design and has been used for a multitude of testing using various turbomachinery components. Additional details, descriptions and testing methods for the Virginia Tech Transonic Wind Tunnel Facility are seen in Nasir et al. [52], Arisi et al. [53], Carullo et al. [54], Holmberg and Diller [55], and Roy et al. [56], as well as others.

B. Test Section, Flow Conditions, and Vane Geometry

Figure 2 displays the linear cascade used for testing, consisting of 4 equally spaced NGV profiles, and half-profiles residing at the top and bottom of the test section. A tailboard is mounted downstream of the top two vane passages to ensure flow periodicity. Mainstream flow enters the test section through a turbulence grid that imparts large-scale freestream turbulence with 16% turbulence intensity; consistent with flow leaving the combustor. The assembly, validation, and usage of the passive turbulence grid is described more thoroughly by Nix et al. [57]. The test section is instrumented with a pitot-static probe, located 2.8 C_{ax} upstream of the leading edge, and 12 static pressure ports on the endwall, 6 at 1.4 C_{ax} upstream of the vane leading edge and 6 at 1.4 C_{ax} downstream of the vane trailing edge, for the passage of interest. A total temperature thermocouple probe measures flow temperature entering the test section at 4.6 C_{ax} upstream of the vane leading edge. All test section pressure measurements were obtained using a NetScanner Model 98RK Pressure Scanner at a frequency of 10 Hz, and temperature measurements using a National Instruments Compact Data Acquisition System at a recording frequency of 30 Hz.

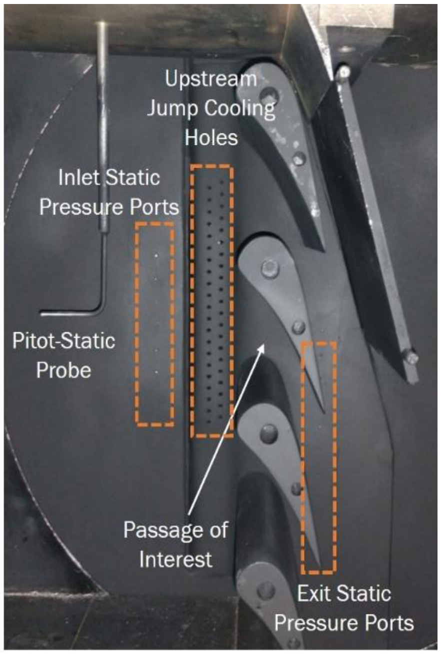

Figure 2. Full Instrumented Test Section with Vane and Endwall Geometry

The vane and endwall geometry were scaled up by a factor of 1.5 and manufactured using a 3D printer and ABSPlus-P430 (acrylonitrile butadiene styrene) as the working material, due to its advantageous thermal and structural properties. The Stratasys Fortus 250mc printer illustrated printing tolerances well within the needed bounds for this experiment. Following manufacturing, the vanes were sanded with incrementally increasing grid count sandpaper before employing an acetone smoothing technique to the surface. The combination ensured the vane geometry was smooth enough for minimal flow disturbances due to surface roughness. All interfaces were sealed using epoxy and sanded to ensure no leakage occurred and smoothness was maintained. Prior to testing, an ultra-flat black paint was carefully applied resulting in an emissivity of 0.97 at 5μm wavelengths. The endwall profile is that of an inner endwall with upstream geometry representing a commonly found gap created by the combustor and vane interface at 0.9 C_{ax} upstream of the vane leading edge. A doublet staggered purge jet cooling scheme centered at 0.38 C_{ax} upstream with an injection angle of 50° from the horizontal, is studied. To ensure coolant hole diameter accuracy and smoothness, each injection hole was carefully bored, and a metal tube inserted and fastened. Figure 3 shows a pitchwise view of the endwall geometry with highlighted coolant flow paths and plenum, while Table 1 outlines the vane geometry, coolant hole geometry, and mainstream flow conditions.

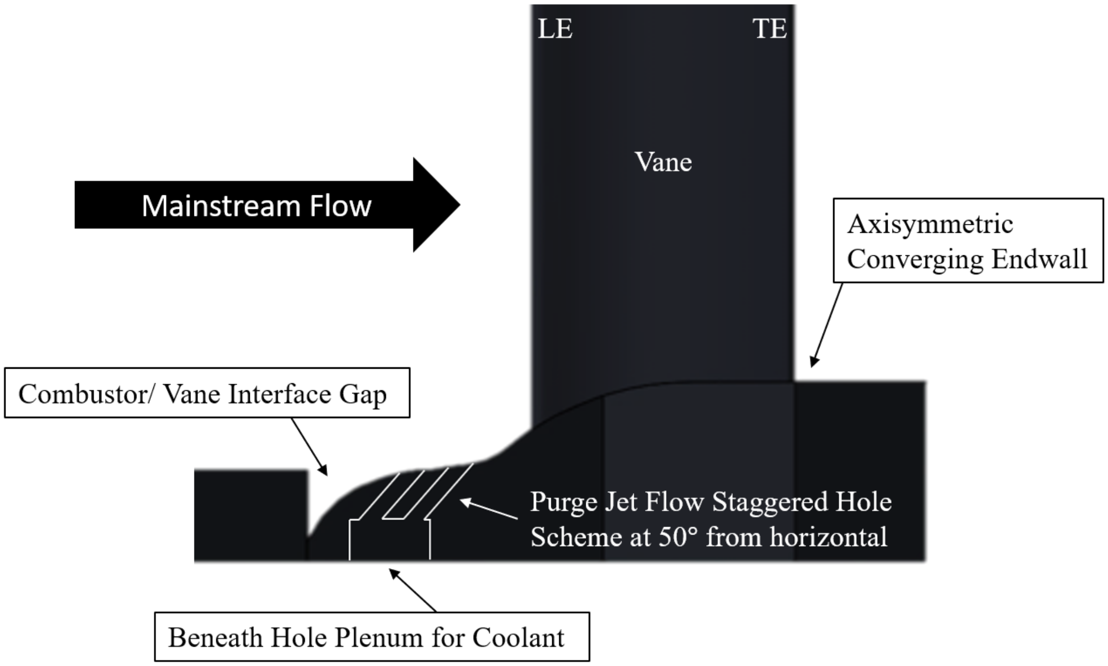

Figure 3. Pitchwise View of Endwall Profile and High Injection Purge Jet Cooling Scheme

Mainstream Flow Conditions	
Inlet Mach Number, $\mathrm{Ma}_{\mathrm{Inlet}}$	0.10
Exit Mach Number, $\mathrm{Ma}_{\mathrm{Exit}}$	0.85
Turbulence Intensity, Tu	16 %
Exit Reynolds Number, $\mathrm{Re}_{\mathrm{Exit,C_{ax}}}$	1.5×10^{6}
Vane and Endwall Geometry	
Endwall Profile	Inner Endwall
Axial Chord, $\mathrm{C_{ax}}$	50 mm
True Chord, C	91.2 mm
Vane Pitch, $\mathrm{P_{Vane}}$	83.1 mm
Inlet and Exit Angle, θ	0° and 73.5°
Cooling Hole Geometry	
Injection Angle, α	50° from Horizontal
Coolant Hole Diameter, $\mathrm{D_{Hole}}$	2.39 mm
Coolant Hole P/D	3.5
Coolant Hole L/D	1st Row – 5.3, 2nd Row – 6.0

Table 1. Mainstream Flow Conditions and Endwall, Vane, and Coolant Hole Geometry

C. Non-Dimensional Coolant Flow Parameter Description and Relevance

For this investigation, coolant density and blowing rate are independently varied to investigate the effect of each on endwall heat transfer and film effectiveness for a nozzle guide vane platform. By varying coolant blowing rate and density, necessarily the coolant momentum and mass flow are altered. All non-dimensional coolant flow parameters of interest, listed in Equations 1 – 4, are calculated at hole entrance, and reported as the mean across all coolant holes.

$$\mathrm{M} = \frac{\rho_c V_c}{\rho_\infty V_\infty}$$

Equation 1. Blowing Ratio

$$\mathrm{DR} = \frac{\rho_c}{\rho_\infty}$$

Equation 2. Density Ratio

$$\mathrm{MR} = \frac{\rho_c V_c^2}{\rho_\infty V_\infty^2}$$

Equation 3. Momentum Ratio

$$\mathrm{MFR} = \frac{\dot{m}_c}{\dot{m}_\infty} \quad \Longrightarrow \quad \mathrm{MFR} = \frac{\rho_c V_c A_c}{\rho_\infty V_\infty A_\infty}$$

Equation 4. Mass Flow Ratio

The non-dimensional coolant parameters are coupled, and highly dependent on one another. Increasing coolant blowing rate for a given density increases both coolant momentum, and mass flow ratio. Observations in film cooling literature conclude this favorably effects endwall secondary flow suppression, but at a critical point, increasing coolant blowing rate leads to jet lift-off and an associated effectiveness decrease, particularly near injection. Conversely, increasing coolant density for a given blowing rate has no effect on coolant mass flow, but largely effects coolant momentum ratio due to an inherent reduction in coolant jet velocity. Reduced coolant momentum results in better film attachment, due to a reduction in a squared coolant velocity term, but is often largely dominated by secondary flows, as cited by many film cooling publications.

While individually, each non-dimensional coolant flow parameter described has been thoroughly studied, a stark lack of simultaneous investigation of multiple parameters is evident, particularly for purge jet cooling. This study simultaneously studies the effects associated with coolant density, coolant momentum, and coolant mass flux, decoupling and identifying the effects of each.

D. Purge Flow Supply and Control

To investigate coolant density, two coolant densities were chosen: DR = 1.2, corresponding to commonly observed experimental neglect of coolant density, and DR = 1.95, representing actual coolant to mainstream density ratios found in engine. For the low coolant density case, compressed air was used as the secondary coolant fluid. High coolant density was achieved by the controlled mixing of Sulfur Hexafluoride (SF_6) and compressed air. Teekaram et al. [58] was a pioneering study showing the validity of using foreign gas and foreign gas mixtures to simulate high density coolant. Two independent plumbing branches were employed to control each constituent independently, ultimately enabling control of the overall coolant mass flux and density. Each branch was independently regulated and fed by a 100 gallon buffer tank filled with compressed dry air at 120 psi, and a Size 200 specialty gas cylinder housing industrial grade SF_6. Lambda Square beveled and corner-tapped orifice plates, Omega Engineering T-Type thermocouples, and pressure measurements upstream and downstream of the orifice were employed to calculate the coolant mass flow in each line simultaneously according to ISO 5167: Part 2, which accounts for all compressibility and expansibility factors in the orifice measurement. The calculated mass flow in each coolant line can then be summed, following conservation of mass, to yield the total mass flow in the complete coolant system. The low-density coolant used only air to meet the mass flow requirements, and the SF_6 line was isolated from the coolant system. Along the coolant flow path 3 static mixers are used to ensure minimal gas stratification occurs before continuing into an equalizing plenum. Three temperature and pressure measurements are made in the plenum via static pressure taps and embedded thermocouples, just before cooling hole entrance, for accurate coolant density calculations. To avoid pre-cooling of the endwall, coolant injection is controlled by a solenoid that is triggered by mainstream pressure.

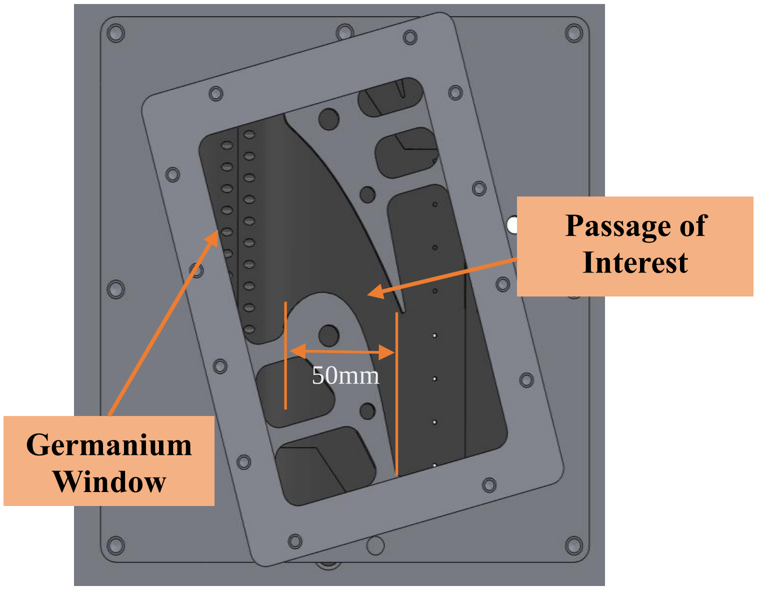

Figure 4. 3D Model of Camera Viewing Plane Through the Germanium Optical Window

E. IR Thermography

A FLIR A325sc model camera was used to accurately track the endwall surface temperature in the spectral range of 7-13 µm wavelengths at a 30Hz sampling rate. The IR camera viewed the endwall through a Germanium (Ge) optical window with a broad band anti-reflective coating which demonstrated an average optical transmission of 95% in the wavelengths of interest. Figure 4 shows a three-dimensional model of the optical window, mounting assembly, and passage of interest from the perspective of the IR camera during testing. Prior to usage, the camera was calibrated and certified by the manufacturer. To account for all effects related to the three-dimensional endwall and Germanium optical window, the IR camera was calibrated for a 75 – 155°F temperature range through the window using surface mounted thermocouples on the upstream (furthest from window) and downstream (closest to window) sections.

Data Reduction Techniques

A. Heat Flux Calculation

The endwall heat flux is calculated as a function of time for each spatial location using the endwall surface temperature measurement, gathered by the IR camera, and the method developed by Cook and Felderman [59]. This method utilizes a one-dimensional semi-infinite conduction model that assumes uniform initial conditions throughout the medium. Additionally, it is assumed that the thermal properties of the medium do not appreciably change due to the subjected temperatures. These assumptions are made possible by the low thermal conductivity of ABSPlus-P430 (k = 0.188 W/mK), which the vanes and endwall are made of, the short window used for data reduction (7 seconds total), and the relatively large thickness of the endwall. This method avoids difficulties traditionally associated with integrating at the upper limit and is easily computable. Equation 5 shows the governing equation for this method.

$$q_n''(t_m) = \frac{2\left(\sqrt{k\rho C_p}\right)_0}{\sqrt{\pi}} \sum_{I=1}^{m} \frac{T(0, t_I) - T(0, t_{I-1})}{\sqrt{t_m - t_I} - \sqrt{t_m - t_{I-1}}}$$

Equation 5. Cook and Felderman Numerical Technique

This method is compared with other traditional methods in [59] and found to compare well while using only a fraction of the computational resources. It is observed that the heat flux is more directly influenced by the shape of the temperature and time relationship at or near the time step of calculation, rather than the temperature and time relationship at the far temporal extrema. This indicates that the accuracy of this technique is dependent upon the ability to approximate the temperature and time curve using a discrete number of straight-line segments connecting each data point gathered. An IR camera sampling rate of 30 Hz is employed to ensure a sufficient number of data points are gathered. Due to the assumption that the initial temperature throughout the medium is constant and the need for the temperature in time profile, the window of calculation for heat flux starts at the start of the tunnel run (includes transient aerodynamic effects), and extends until the end of the reduction window for the Dual Linear Regression Technique (see Figure 5).

B. Dual Linear Regression Technique (DLRT)

The recovery temperature (T_r), heat transfer coefficient (HTC), and adiabatic film cooling effectiveness (η) are calculated simultaneously by the Dual Linear Regression Technique (DLRT) outlined in Xue et al. [60]. The governing equation for this technique, Equation 8, is a linearized combination of the definition of HTC for a film cooled surface, Equation 6, and the definition of adiabatic film cooling effectiveness, Equation 7, where HTC is the slope and η is the quotient of the y-intercept divided by the slope.

$$\mathrm{HTC} = \frac{q''}{T_{aw} - T_w}$$

Equation 6. Definition of Heat Transfer Coefficient for a Film Cooled Surface

$$\eta = \frac{T_r - T_{aw}}{T_r - T_c}$$

Equation 7. Definition of Adiabatic Film Cooling Effectiveness

$$\begin{array}{cccccc} \dfrac{q''}{T_r - T_c} & = & \mathrm{HTC} & \left(\dfrac{T_r - T_w}{T_r - T_c}\right) & - & h\eta \\ \downarrow & & \downarrow & \downarrow & & \downarrow \\ y & = & m & x & + & b \end{array}$$

Equation 8. Linearized Governing Equation for DLRT

The window of calculation for this method is chosen to avoid transient aerodynamic conditions and lasts only several seconds to preserve all assumptions (≈5 seconds). Figure 5 displays how the reduction windows for all calculations are dispersed across a typical experiment as they relate to mainstream exit Mach number, mainstream temperature, and coolant temperature,

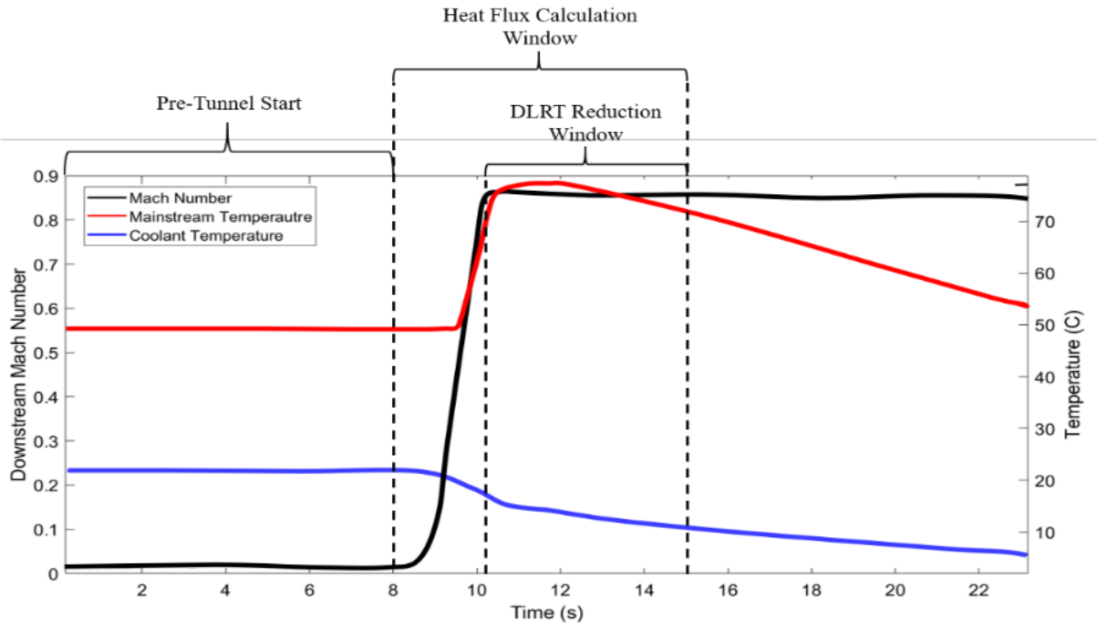

Figure 5. Reduction Window Display for All Reduction Techniques

$$T_r = T_{T,\infty}\left(\frac{1 + r\dfrac{\gamma - 1}{2}Ma^2}{1 + \dfrac{\gamma - 1}{2}Ma^2}\right) \rightarrow T_r = T_{T,\infty}C_r$$

Equation 9. Definition of Recovery Temperature

for one of the two test runs needed. This method relies upon a dispersion of data points to minimize regression uncertainty. To ensure this, two experimental runs are conducted with the same aerodynamic, blowing, and mainstream thermal conditions in the reduction window. The coolant temperature is chilled in one case and ambient in the other. HTC, η, and the recovery coefficient, C_r, are hydrodynamic parameters and remain constant across both runs with the preservation of aerodynamic and blowing conditions in the reduction window. Equation 9 describes the definition of recovery temperature, T_r, and coefficient, C_r, as related to mainstream conditions.

The calculation method is an optimization of R^2 for the linear regression of Equation 8 for both the chilled and ambient coolant test runs simultaneously. R^2 is a statistical measure of the proportion of variance for a dependent variable explained by an independent variable. For this, physically plausible recovery coefficient values (1 - 0) are iterated through for each pixel. For each

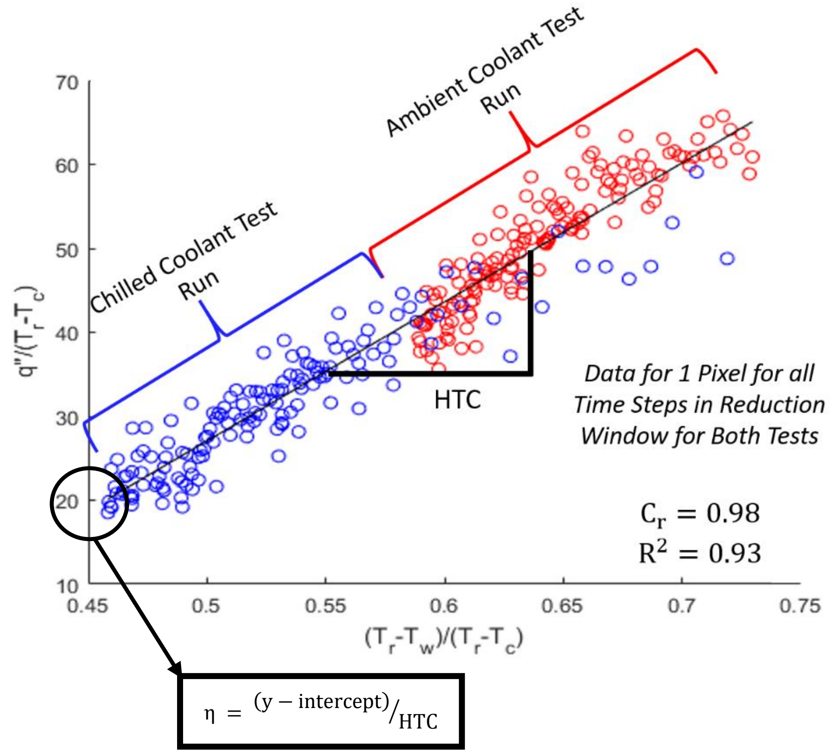

Figure 6. Converged Solution for the DLRT Model for a Single Pixel

value the x-axis and y-axis parameters shown in Equation 8, for each temporal step in the reduction window, are calculated and linearly regressed. The linear regression yields HTC, η, and R^2, which is stored with the corresponding C_r value for a given pixel. The recovery coefficient corresponding to the highest R^2, with physically plausible HTC and η values, is taken as the approximate solution. A finer mesh of C_r values is determined by, and encompasses, the approximate solution. The same steps are repeated to come to a solution of sufficiently more accuracy than the first approximate solution. These steps are repeated until the desired accuracy of C_r is met for a given spatial location. The process is completed for all pixels, or spatial locations, captured by the IR camera. During each calculation process all parameters are monitored with specific criterion to mitigate convergence on a singular region as described in Xue et al. [60]. An example of a converged solution for a given pixel is illustrated in Figure 6 with the associated C_r and R^2 values.

C. Net Heat Flux Reduction

Commonly in gas turbine heat transfer, a paradox exists in that often the injection of fluid to shield the endwall from high velocity and temperature gases imparts additional turbulence into the flow and augments heat transfer coefficient. This implies that coolant effectiveness could be high even in areas where HTC is increased. For this, the gas turbine heat transfer and film cooling research community attempted to account for all effects in a single umbrella parameter, Net Heat Flux Reduction (NHFR). NHFR evaluates the reduction of endwall heat flux with the introduction of coolant, intrinsically accounting for augmented heat transfer coefficient at injection and decreased surface temperature due to effective film cooling. More information on Net Heat Flux Reduction is given in Lynch and Thole [61], Li et al. [62], Sen et al. [63], and Roy et al. [64]. NHFR is described by an analytical expression combining the adiabatic film effectiveness and HTC for the cooled case, and the HTC for the uncooled case. This is shown in Equation 10, with further definition of overall film effectiveness in Equation 11 and following.

$$\mathrm{NHFR} = \frac{q''_{w,uncooled} - q''_{w,f}}{q''_{w,uncooled}} \rightarrow \mathrm{NHFR} = 1 - \frac{\mathrm{HTC}_f}{\mathrm{HTC}_{uncooled}}\left(1 - \frac{\eta}{\varphi}\right)$$

Equation 10. Net Heat Flux Reduction

$$\varphi = \frac{T_r - T_w}{T_r - T_c}$$

Equation 11. Overall Film Effectiveness

Mick and Mayle [65] state that considering a realistic turbine inlet temperature, coolant temperature, and component temperature for typical gas turbine engines, an average overall cooling effectiveness (φ) is 0.6, which is employed for this study.

Uncertainty Analysis

The uncertainties for the calculations of heat transfer coefficient and adiabatic film cooling effectiveness were examined using Moffat's perturbation method [66], which expand upon the ideas of Kline and McClintock [67]. For this method, HTC and η were reduced to the primary measured variables used in calculation: mainstream temperature, coolant temperature, and endwall surface temperature. The mainstream temperatures were monitored with a T-Type thermocouple total temperature probe, and the coolant with three T-Type fast-response exposed junction embedded thermocouples. The reported uncertainty for T-Type thermocouples is ±1.0℃ or ±0.75% of the reading, whichever is greater. The endwall surface temperature measurement uncertainty is ±2.0℃ or ±2.0% of the reading, whichever is greater, as reported for the afore mentioned FLIR A325sc IR camera used. All uncertainties were applied to their respective measurements in the additive and subtractive manner. Each possible combination of uncertainties, both individual and simultaneous, were used to calculate the subsequent HTC and η values. This analysis yielded a maximum uncertainty of ±9.6% in HTC, and ±0.1 in η. These uncertainty calculations are valid only for regions where the one-dimensional semi-infinite conduction model is applicable and does not consider regions where this model fails.

The freestream exit Mach number, coolant to mainstream blowing ratio, and coolant to mainstream density ratio are all important parameters in this testing, and as such are monitored and ensured to be within acceptable bounds. The freestream exit Mach number for each test case was kept within ± 5% of the defined condition of 0.85 for each test case. A maximum deviation of 6% from ideal conditions was observed for blowing ratio and density ratio, with an average deviation across all tests of 3% for both. This gives good confidence that the aerodynamic and blowing conditions were nearly constant across the two runs needed for the Dual Linear

Regression Technique, and that all observed differences are due to the varied parameter of interest, coolant blowing rate or density.

Results and Discussion

The experimental testing results for this study are arranged in the following manner: First, gathered results are compared with a relatable test in open literature to further validate data trends. Secondly, the effect of coolant density is investigated with regards to adiabatic film cooling effectiveness and endwall heat transfer distributions for coolant blowing rate of 2.5 and 3.5 (M = 2.5 and M = 3.5). Upstream and in-passage characteristics will be analyzed separately, and a full comparison between coolant densities presented. Finally, the effect of coolant mass flux at two levels, which correspond to engine extrema (M = 2.5, and M = 3.5), is examined at engine representative coolant to mainstream density ratio. Qualitative conclusions will first be drawn using oil flow visualization techniques, before again employing adiabatic film cooling effectiveness and endwall heat transfer distributions for comparison. Both local and full passage effects are considered and discussed. For this study, the endwall heat transfer is analyzed using Nusselt Number (Nu), a nondimensional quantity representing heat transfer coefficient (HTC), for better comparison with literature, and Net Heat Flux Reduction (NHFR). A comprehensive test matrix for this study can be seen in Table 2 with the associated coolant flow parameters. Mainstream conditions were held consistent with those reported in Table 1 for all test cases.

Test Conditions	M	DR	MR	MFR
Low Blowing, Low Density Ratio Condition	2.50	1.20	5.21	2.00
Low Blowing, High Density Ratio Condition	2.50	1.95	3.21	2.00
High Blowing, Low Density Ratio Condition	3.50	1.20	10.21	2.80
High Blowing, High Density Ratio Condition	3.50	1.95	6.28	2.80

Table 2. Experimental Test Matrix (Engine Design Condition Highlighted)

A. Comparison with Relevant Literature

There are no current studies in open literature that utilize a purge jet cooling scheme while matching engine representative coolant and mainstream conditions. Li et al. [51] provides the most relatable in an analysis of cooling through a single row of tightly spaced, low diameter cooling holes in a similar endwall position as typically found for a purge jet cooling scheme. The tests are conducted at low speed and low turbulence conditions on a flat endwall, with coolant to mainstream blowing ratio and density ratio varied between 1.3 – 2.2 and 1.0 – 1.52 respectively. The results are compared with results from the current study in Figure 7. The color scheme for the current study contours has been altered to be consistent with the comparable study, but the limits remain different.

The overarching trends are similar between the two studies, but differences in geometry and flow conditions largely affects the adiabatic effectiveness magnitudes. The high density coolant exhibits superior film cooling performance near-hole, due to better coolant attachment, but quick degradation into the passage. The low density coolant results in greater coolant lift-off from the surface and subsequent decreased film effectiveness near-hole. Upon reattachment, the low density coolant further penetrates the passage providing better in-passage film cooling effectiveness, particularly near the pressure side trailing edge. The validation of data trends with increasing coolant density amid different experimental conditions, while using a different techniques, give the author good confidence in the results presented herein.

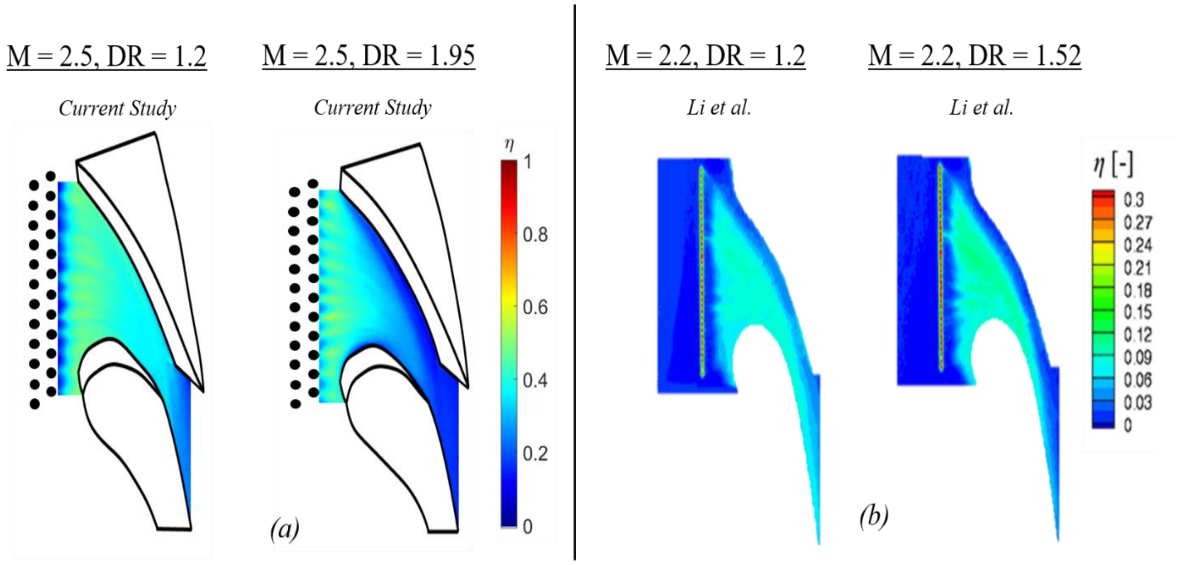

Figure 7. Comparison of η Between the Current Study *(a)*, and Li et al. [51] *(b)*

B. Effect of Density Ratio on Film Performance and Endwall Heat Transfer

Adiabatic Film Effectiveness:

The effect of coolant density for the low blowing condition, M = 2.5, on film effectiveness is illustrated through the endwall adiabatic film cooling effectiveness distributions in Figure 8. Three regions of interest are labeled: Region A, corresponding to the upstream near-hole region, Region B, corresponding to the near PS region, and Region C, corresponding to the near SS region. The three regions identified will be the talking points for the following paragraphs.

In Region A, large film effectiveness enhancements are observed with elevated coolant density, particularly following injection site, indicating superior film attachment. This is attributed

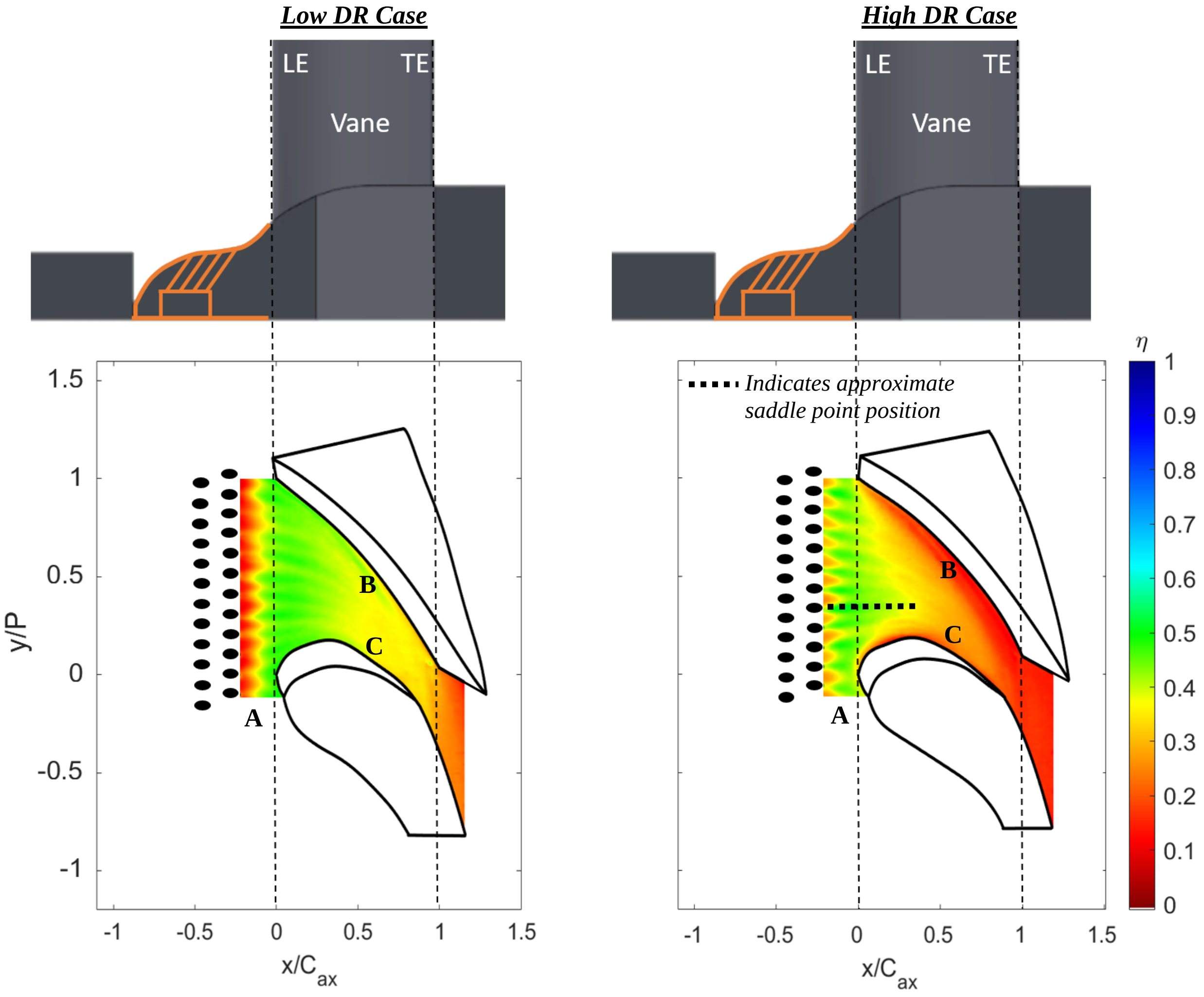

(a) *(b)*

Figure 8. η Contour for M = 2.5 and DR = 1.2 *(a)*, and DR = 1.95 *(b)*

to the 42% decrease in coolant momentum with increased density, acting to facilitate better film attachment following injection. The high density low momentum coolant jets are clearly influenced by the endwall secondary flows due to the jet direction variation in the pitchwise direction. All jets are influenced toward the saddle point at 0.35 $^{y}/_{P}$, influence growing with pitchwise direction. Conversely, the low density coolant lifts from the endwall, creating a region of low effectiveness extending from injection to -0.15 C_{ax}. Evidently, the combination of jet reattachment, favorable pressure gradient, staggered array of cooling holes, and endwall contouring aid in laterally spreading the low density coolant across the endwall near leading edge once reattached, facilitating near uniform effectiveness values at -0.05 C_{ax}.

Large variations in film cooling performance across tested coolant densities are apparent when progressing into the passage, particularly in Regions B and C. This is attributed to the PS and SS horseshoe vortex domination of the high density coolant flow. The PS HSV sharply decreases effectiveness from leading edge to saddle point in the pitch-wise direction at 0.5 C_{ax}, Region B. The uncooled region grows with progression downstream due to the sweeping of coolant across passage, leaving the regions near the pressure side trailing edge largely uncooled. Near suction side, Region C, the high density coolant is unable to penetrate or suppress the SS horseshoe vortex system, leaving a small uncooled region from leading edge to 0.5 C_{ax}. Comparatively, the high coolant moment for the low density condition provides enhanced film effectiveness in Regions B and C due to suppression of secondary flows. This trend continues through the throat of the passage with the low density coolant exhibiting improved film effectiveness at PS trailing edge and a more even distribution in the throat. Further in-passage penetration for low density coolant is owed to increased coolant momentum, reducing endwall pressure gradients and crossflows.

Figure 9 shows the adiabatic film cooling effectiveness distributions for both coolant densities tested at the elevated blowing condition, M = 3.5. A similar analysis is conducted with areas of interest again marked in the upstream near-hole region, the near PS region, and the near SS region. Both cases have sufficient momentum to cause jet lift-off from the surface, creating regions of low film effectiveness downstream of the cooling holes. The coolant reattachment zone, starting at -0.125 C_{ax}, is comprised of relatively lower effectiveness cooling streaks as compared to the M =2.5, DR = 1.2 case, which also exhibited jet-lift off. This is attributed to augmented mixing caused by increased levels of turbulence, and the lack of definite coolant reattachment. Lift

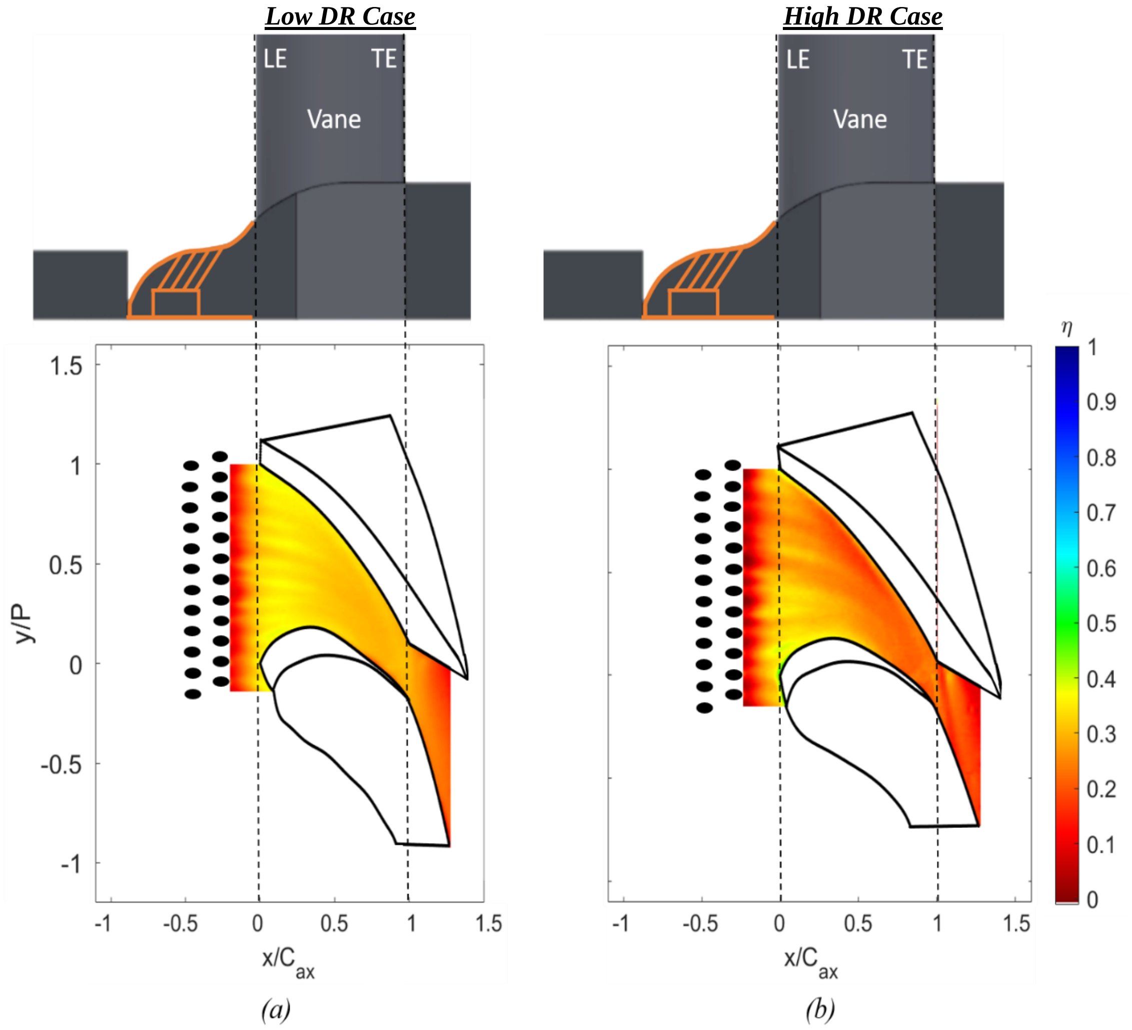

(a) *(b)*

Figure 9. η Contour for M = 3.5 and DR = 1.2 *(a)*, and DR = 1.95 *(b)*

off is significantly augmented for the high blowing condition due to a 96% and 21% increase in momentum for the low and high density coolant conditions respectively. In Region A, the trends and magnitudes across both coolant to mainstream density ratios are similar. For the high blowing high density case, the effectiveness is further decreased in Region B, attributed to the formation of the pressure side horseshoe vortex system, which has significantly shifted downstream and is noticeably weaker as compared to the M = 2.5, DR = 1.95 case. This is indicative of the increased coolant momentum marginally suppressing and shifting the flow structure. The low effectiveness region for the high density coolant case is carried across the passage near the throat, owed to the PS HSV migration across passage, forming the passage vortex. Upon formation, the passage vortex entrains much of the coolant at mid-passage near throat, leaving Region C with little film

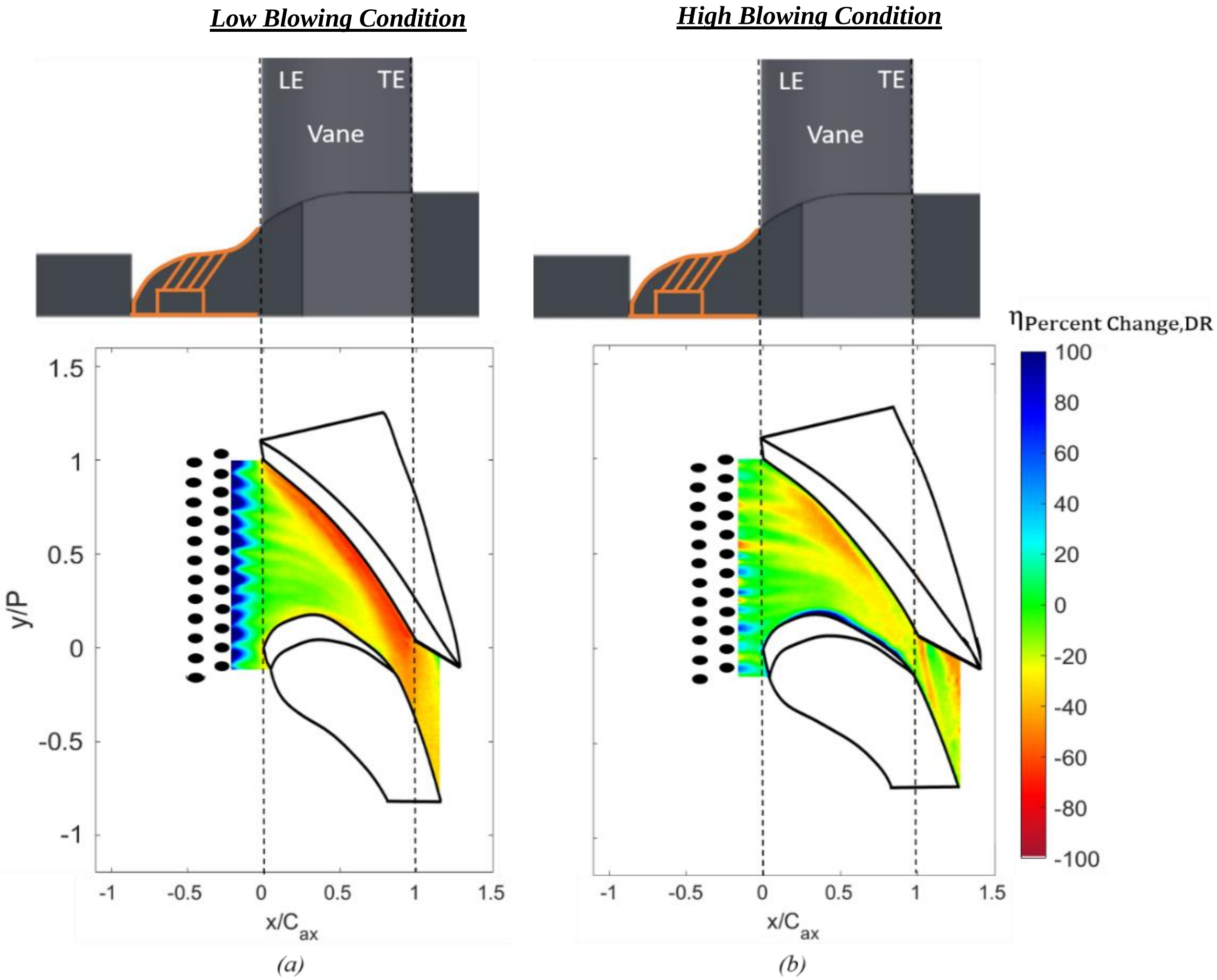

Figure 10. Percent η Change Due to DR Increase for M = 2.5 *(a)*, and M = 3.5 *(b)*

effectiveness. Comparatively, the low density coolant provides more uniform effectiveness throughout the passage following reattachment. The increased coolant momentum is able to overcome the adverse pressure gradient, and no coolant shortage or decreased effectiveness region is observed near Region B. Pressure side horseshoe vortex suppression and reduction of cross-passage velocity, due to enhanced coolant momentum, result in a better endwall shielding in Region C.

To further analyze the effect of coolant to mainstream density ratio on adiabatic film effectiveness, the percent change in η due to increased density ratio, defined in Equation 12, is reported for both blowing rates tested in Figure 10.

$$\eta_{\text{Percent Change,DR}} = \frac{\eta_{\text{HDR}} - \eta_{\text{LDR}}}{\eta_{\text{LDR}}} \times 100\ \%$$

Equation 12. Percent η Change due to Increased Coolant Density

This analysis illustrates regions with large variations in film effectiveness due to increased coolant density. Positive regions (navy blue, royal blue and teal) indicate a facilitation of better film effectiveness and negative regions (red, orange, and yellow) indicate adverse film effectiveness alteration, due to increased coolant density. Evidently, coolant density has a more pronounced effect for the low blowing condition. It is observed that in both cases the pressure side is difficult to cool, particularly near trailing edge, for the high density coolant, due to decreased momentum. For the high density low blowing condition, near hole effectiveness is increased by more than 100%, but near PS effectiveness suffers approximately a 35% reduction in film effectiveness. For the high blowing condition, visible streaks of decreased effectiveness are apparent at the coolant reattachment zone near PS. These streaks are attributed to the adverse pressure gradient suppressing reattachment effects for the high density coolant but having near no effect on the low density coolant. The area most adversely affected by the high density coolant is near PS for the low blowing condition, attributed to the entrainment and domination of the coolant by the pressure side horseshoe vortex system. Results indicate that neglecting coolant density could lead to overlooked thermal hotspots, elevating the risk of thermal failure.

Endwall Heat Transfer:

The following sections investigate the effect of coolant density on endwall heat transfer. Endwall Nusselt number augmentation and Net Heat Flux Reduction contours are employed to illustrate the local and overall changes. $\text{Nu}_{\text{Augmentation,DR}}$, described in Equation 13, shows the percent change on endwall Nusselt number due to increased density coolant.

$$\text{Nu}_{\text{Augmentation,DR}} = \frac{\text{Nu}_{\text{HDR}} - \text{Nu}_{\text{LDR}}}{\text{Nu}_{\text{LDR}}} \times 100$$

Equation 13. Percent Nusselt Number Change Due to Increased Coolant Density

In regions of positive augmentation, corresponding to red, the endwall Nu is raised with coolant density elevation. In negative augmentation regions, corresponding to blue, a reduction of endwall

Nu is observed. Figure 11 shows the $\mathrm{Nu}_{\mathrm{Augmentation,DR}}$ for the low and high blowing conditions. Three regions of interest are identified and marked as Regions A, B, and C, corresponding to the near-hole upstream region, PS region, and SS region respectively. At the low blowing condition, M = 2.5, a transition line is observed at near 0.35 C_{ax}. Prior to the transition line, in Region A, high density coolant lowers the endwall Nu by near 50% as compared to low density coolant, except at the saddle point. The reduction in Nu is attributed to the elevation in coolant density resulting in a proportional decrease in coolant momentum, facilitating improved coolant attachment and coverage downstream of injection site. Higher density coolant forms a layer of

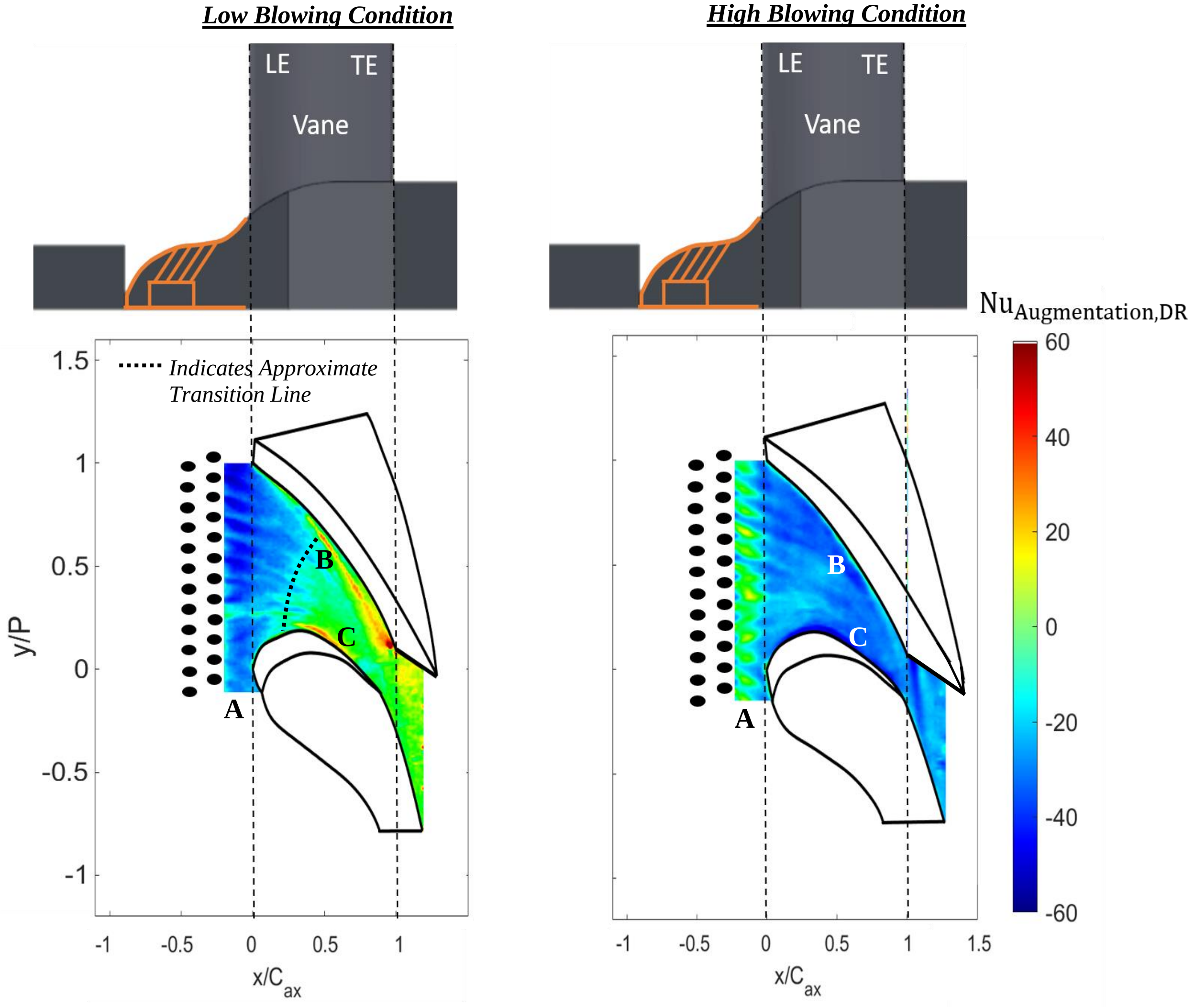

(a)

(b)

Figure 11. Nu Augmentation Due to Increased DR for M = 2.5 (a), and M = 3.5 (b)

relatively slower moving fluid near endwall, acting to shield from the high velocity and turbulent freestream, thereby lowering endwall Nu. Comparatively, the low density coolant has sufficient momentum to lift from the endwall, augmenting endwall Nu due to turbulent mixing of the boundary layer and coolant jets. These differences are not as substantial near saddle point, due to the favorable pressure gradient in this region pushing even high momentum coolant back toward endwall.

These trends are somewhat reversed for the high blowing condition, $M = 3.5$. Increasing density ratio results in a region of near zero augmentation just downstream of the hole in the coolant jet wakes, Region A. At both coolant density conditions the coolant momentum is sufficiently high at this high blowing condition, $M = 3.5$, to lift from endwall and turbulently mix with the mainstream. This results in nearly the same endwall Nu augmentation for both coolant densities, therefore nearly no percent change is observed.

A band of nearly no endwall Nu change exists downstream of the transition line at mid-pitch for the low blowing condition, $M = 2.5$. However, in both Regions B and C, an increased in endwall Nusselt number is observed with coolant density increase. This is a result of the high density and low momentum coolant flow being swept away from PS toward SS before eventual entrainment in the passage vortex. From this, the pressure side, especially near trailing edge is left largely unshielded from the high velocity mainstream. Conversely, the low density coolant at the low blowing condition is permitted to shield Regions B and C, due to an increased coolant momentum. Increased coolant momentum allows for PS and SS horseshoe vortex system suppression and endwall cross flow reduction. This combination allows for coolant to penetrate more near vane/endwall junctions and into the passage, broadening the shielded area. The increase in pressure side trailing edge region Nu for the high density coolant at the low blowing condition is further accentuated by the association of this region with high thermal loads.

Downstream of Region A, a 20 – 30% reduction in endwall Nu is observed with increased coolant density for the high blowing condition. The reattachment and lateral spreading of a slower moving layer of coolant shields the endwall for the high density case. A similar shielding layer is formed for the low density ratio case; however, the layer is moving more quickly near endwall due to a doubling of coolant jet momentum. Thus, the majority of the endwall Nu in passage are reduced with increased coolant to mainstream density ratio. This is less exaggerated near the saddle point due to the inherently favorable flow conditions.

To further analyze the effect of increasing DR on endwall heat load, Net Heat Flux Reduction calculations were employed and illustrated in Figure 12. NHFR is a measure of the heat flux reduced by the introduction of coolant and is the gas turbine heat transfer and research communities attempt to combine all complex factors into a single variable. Regions nearing unity and marked by blue have undergone significant heat flux reduction, while regions marked by red and nearing negative NHFR have not been affected, or are adversely affected, by the introduction of coolant flow.

Across both coolant to mainstream density ratios, the low blowing condition provides significantly elevated NHFR levels. This is attributed to the lack of film coolant reattachment for the high blowing condition, $M = 3.5$, independent of coolant density. The low blowing, low density coolant condition has superior NHFR performance with levels up to 0.8 in typically high secondary flow regions, such as near PS and SS. Lateral spreading upon coolant reattachment combined with the suppression of secondary flows acts to shield the majority of the endwall from the mainstream, reducing the heat flux. Comparatively, the high density, low blowing condition increased NHFR near hole, but performance degrades quickly into the passage. Attachment of coolant downstream of the hole forms a protective boundary reducing the endwall heat flux, however, the attached coolant cannot afford to penetrate deep in-passage due to secondary flow domination and entrainment. This leaves the PS, especially near trailing edge, and throat region more exposed to the high temperature and velocity mainstream. The discrepancy illustrated in Figure 12(a) as compared to Figure 12(b) underlines the distinct need for DR consideration when designing and analyzing a purge jet cooling scheme

Independent of coolant density, the high blowing condition maintains a similar endwall heat flux profile. This is attributed to the momentum effects becoming increasingly dominant at high blowing rates, minimizing the effect of coolant density. Near pressure and suction side are regions of highest heat flux reduction due to the suppression of secondary flow and subsequent penetration of coolant to vane/endwall junction. This is more exaggerated for the high density ratio, high blowing condition due to decreased velocity in the boundary layer. At mid-pitch, from leading edge to 0.5 C_{ax}, a region of reduced endwall NHFR is observed. The increase in endwall heat flux is intensified with migration toward near pressure side regions. Primarily, the complex and intense coolant and freestream interaction create this region. The high coolant momentum present for both cases impart large amounts of free stream turbulence in the upstream region. The

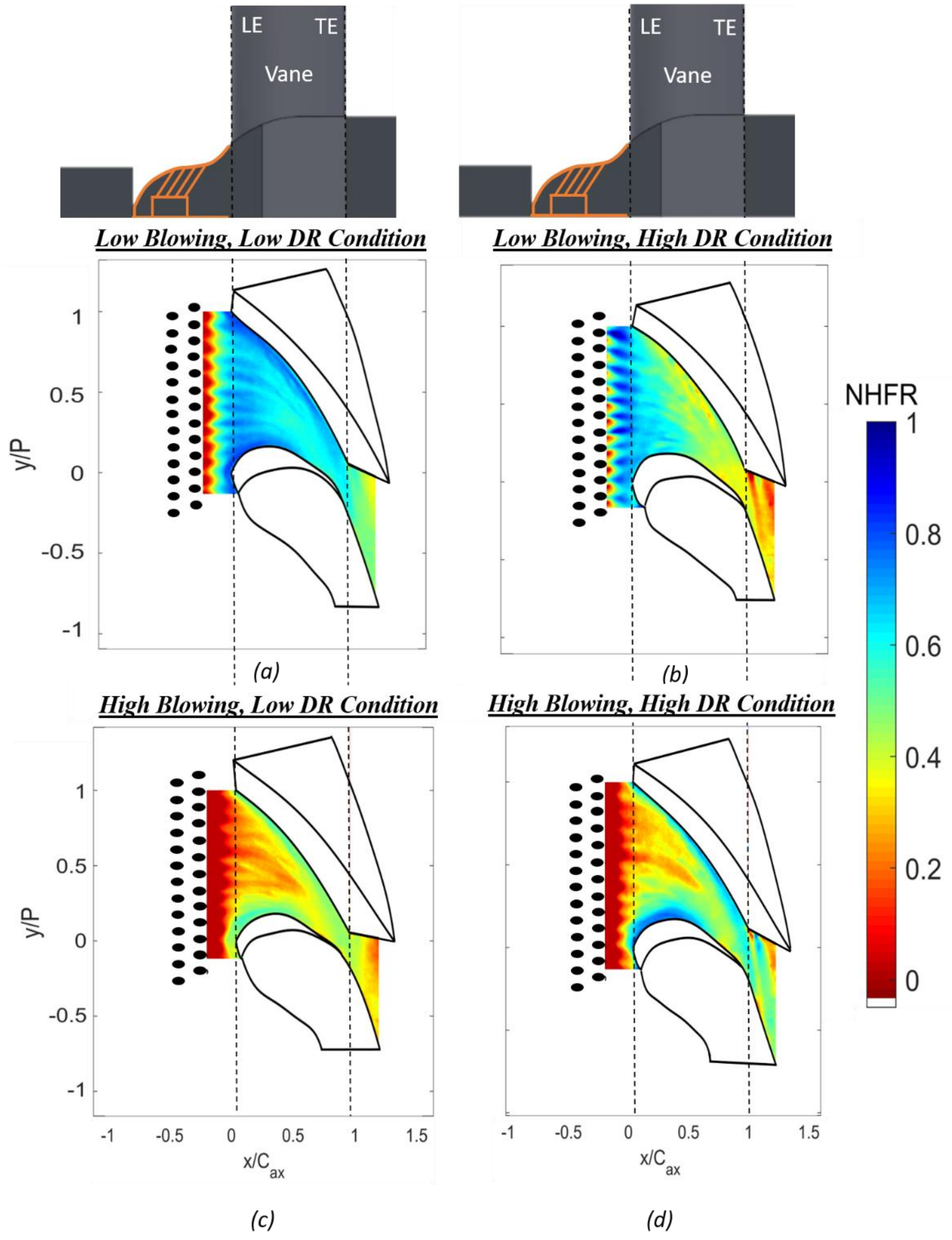

Figure 12. NHFR Contours for M = 2.5 and DR = 1.2 *(a)*, M = 2.5 and DR = 1.95 *(b)*, M = 3.5 and DR = 1.2 *(c)*, and M = 3.5 and DR = 1.95 *(d)*

increased turbulence is most influential at the onset of the passage, and when in combination with low film effectiveness, creates a region of low NHFR. For all conditions tested, when coolant had sufficient momentum to lift from the endwall (low density and low blowing condition, low density and high blowing condition, and high density and high blowing condition) negative regions of Net Heat Flux Reduction were observed just downstream of injection. Severely increased turbulence levels due to coolant and mainstream boundary layer mixing, and a lack of effectiveness due to lift off, are determined to be the causes of this. This implies that the introduction of coolant facilitates greater heat flux into the endwall in the upstream near hole region if sufficient momentum to lift off is acquired.

C. Effect of High Density Coolant Blowing Rate on Endwall Heat Transfer and Film Effectiveness

Oil Paint Flow Visualization:

Before investigating the effects of coolant mass flux on film effectiveness and endwall heat load, it is important to understand the governing flow physics and their respective alterations. For this, oil paint flow visualization techniques were employed and used as a tool to quantitatively analyze endwall flow physics in the presence of low blowing, high density coolant

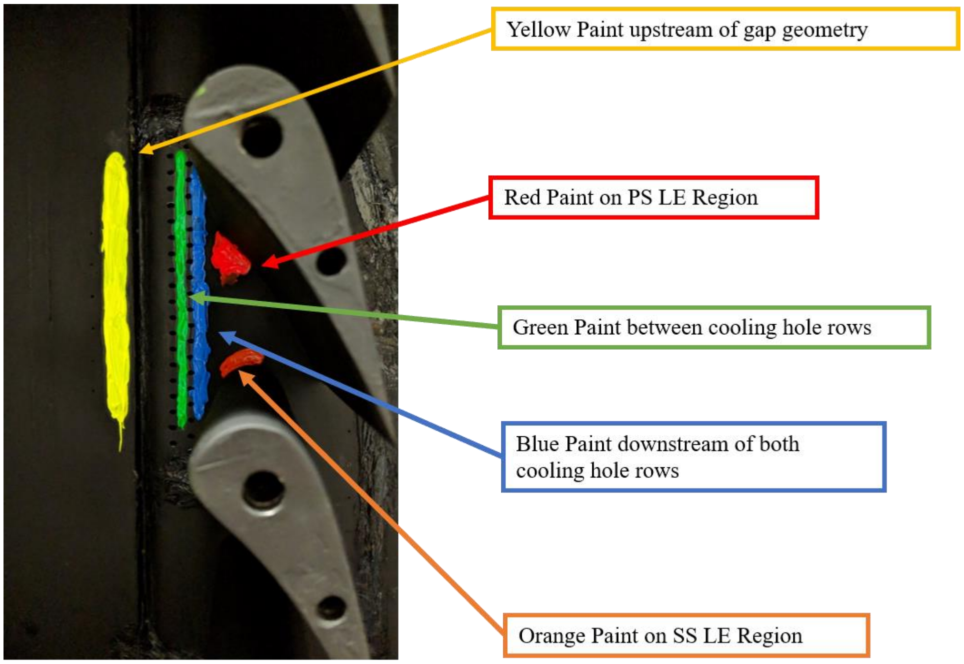

Figure 13. Oil Paint Flow Visualization Application Prior to Blowdown

(M = 2.5, DR = 1.95), and high blowing, high density coolant (M = 3.5, DR = 1.95). Fluorescent paint pigments were mixed with low viscosity (100 cSt) silicon oil and applied to the endwall. Endwall application prior to blowdown is illustrated in Figure 13. Paint was carefully applied in very thin layers to ensure minimal flow disruption. Orange and Red paints were applied to the suction and pressure side leading edge regions respectively, to analyze each leg of the horseshoe vortex system. Yellow, green, and blue paint streaks were applied upstream of vane leading edge to measure the flow features near the upstream gap, between cooling hole rows, and directly

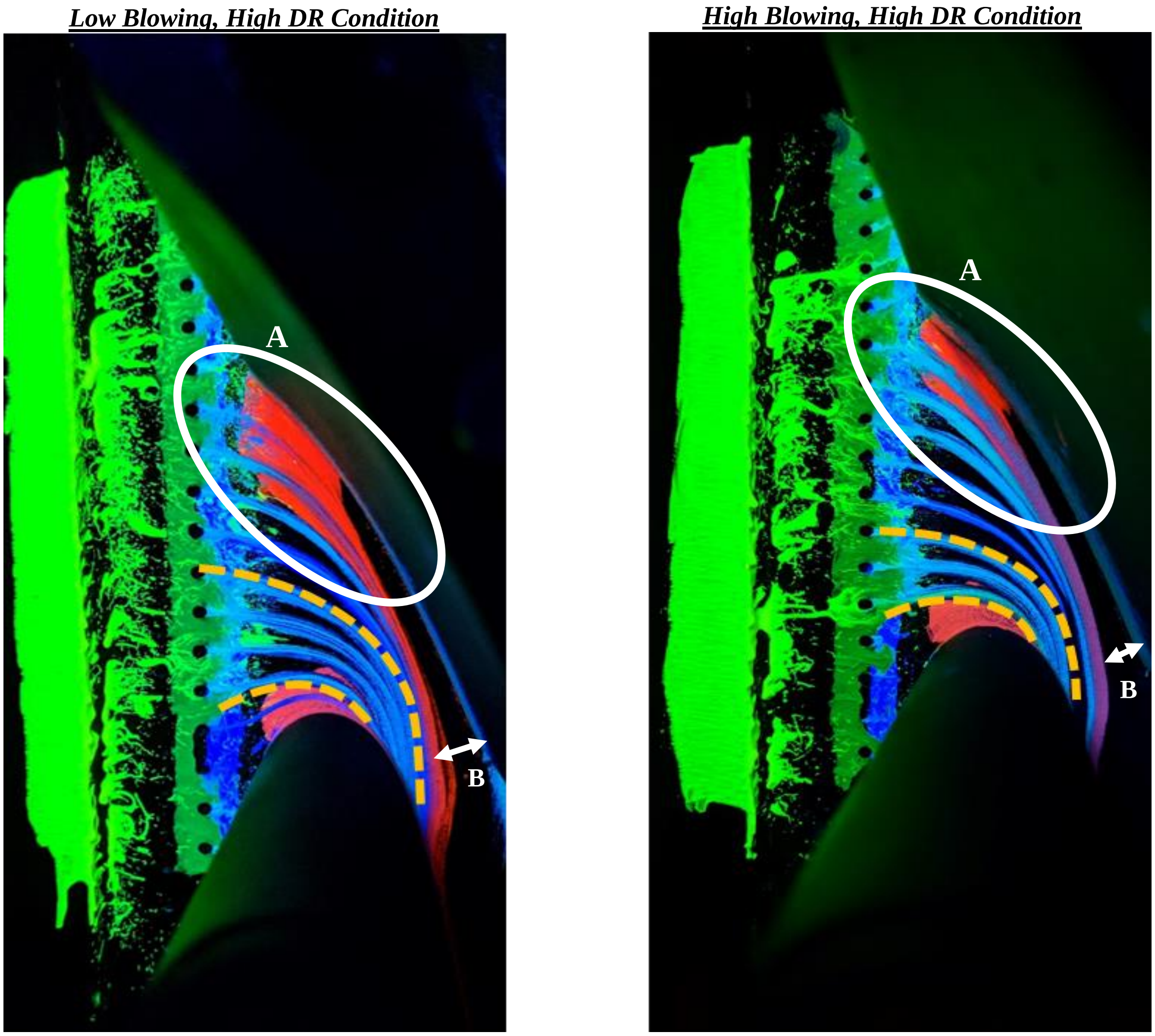

(a)

(b)

Figure 14. Flow Visualization Post Blowdown for High Density Coolant at M = 2.5 (a), and M = 3.5 (b)

downstream of coolant injection. Following application, a test run was conducted for both the high density low blowing condition, and high density high blowing condition.

Figure 14 houses photos of the flow visualization results for both conditions tested amid a UV-A light source. In Region A, blue paint is found nearer to the pressure side endwall/vane junction for the high blowing rate case tested. This is indicative of PS horseshoe vortex system suppression by the cooling jets at higher blowing rates. Further illustrating this is Region B, where the proximity of blue paint to PS trailing edge has decreased significantly with increased blowing. The decrease observed is due to, as noted, PS HSV suppression and further coolant penetration into the passage, reducing cross-stream secondary flow velocity and allowing coolant to reach near pressure side trailing edge. Finally, a narrowing and shifting of the saddle point is observed toward the SS of the adjacent vane with increased blowing. This suggests that the coolant is able to better suppress the suction side horseshoe vortex system with increased blowing, and subsequent increased coolant momentum. These results are consistent in trend with those found in Mahadevan et al. [68] in which similar flow visualization techniques were employed.

Adiabatic Film Cooling Effectiveness:

The effect of blowing rate with engine represented coolant density is investigated on adiabatic film cooling effectiveness with results shown in Figure 15. For this, the percent change in η due to increased high density coolant blowing rate is employed, and shown in Equation 14.

$$\eta_{\mathrm{Percent\ Change,M}} = \frac{\eta_{\mathrm{HM}} - \eta_{\mathrm{LM}}}{\eta_{\mathrm{LM}}} \times 100$$

Equation 14. Percent **η** Change Due to High Density Coolant Blowing Rate Increase

By reporting $\eta_{\mathrm{PercentChange,M}}$, areas with large variation due to increased blowing rate are easily recognizable. Positive regions, areas containing a coloration of some form of blue, are positively influenced by the increase in coolant mass flux in terms of film effectiveness. Conversely, negative regions, containing a color of the red variety, are adversely affected by increasing coolant mass flux.

Very near pressure and suction sides are regions of enhanced film effectiveness due to increased blowing. Near PS this profile of high enhancement starts at vane leading edge and

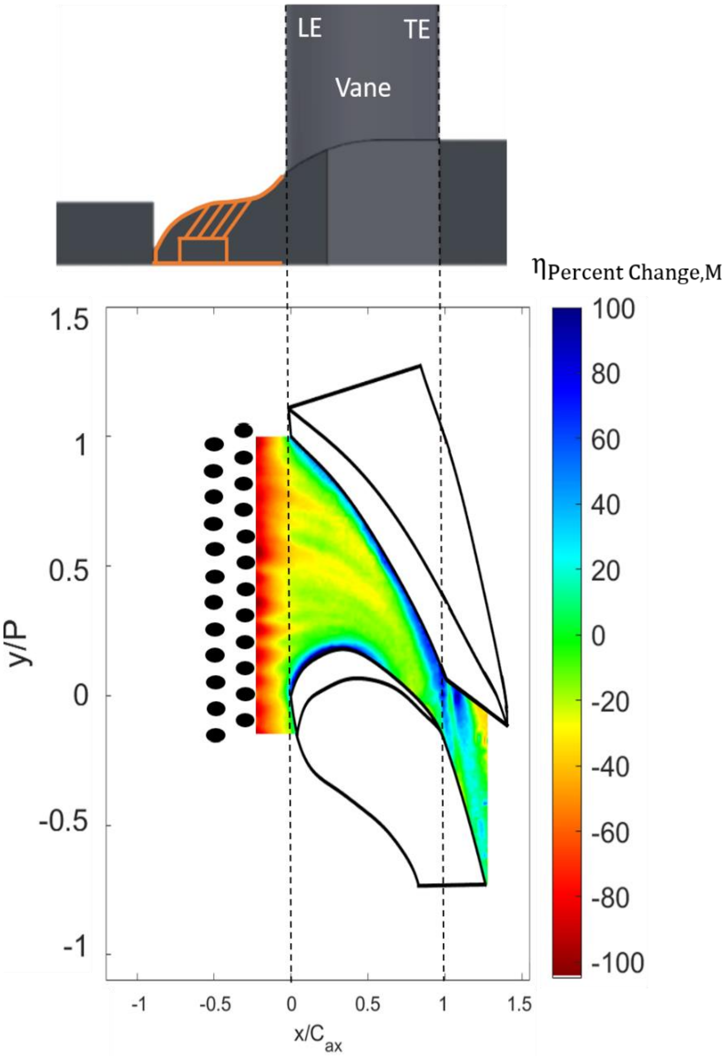

Figure 15. Percent η Change for High Density Coolant Due to Increased Blowing Rate

progressively grows larger through the passage, with the largest region of enhancement at PS trailing edge. This is owed to the increase in coolant momentum due to increased high density coolant blowing rate. The enhanced momentum suppresses the PS HSV, thereby allowing coolant to penetrate closer to the endwall/vane junction. With this suppression, sweeping of the PS HSV across passage is reduced, and the high blowing, high density coolant is permitted to penetrate further into passage. The enhancement observed near suction side is due to similar mechanisms. The high momentum present for the increased blowing rate allows suppression of the SS HSV and facilitates better cooling near the endwall/vane junction. Overall the near pressure and suction side regions are enhanced by 60-80% with increasing high-density coolant blowing rate.

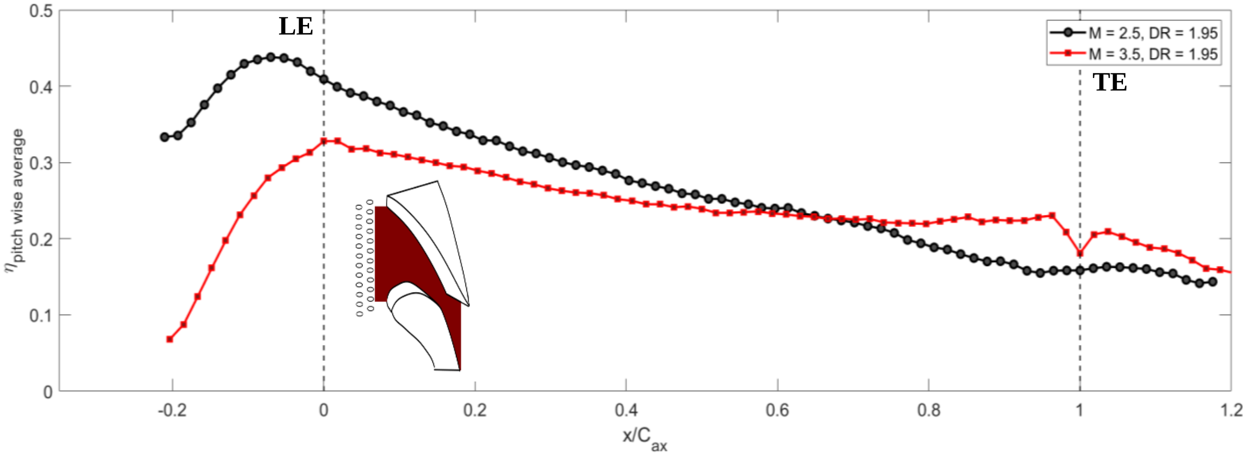

Figure 16. Pitchwise Average η for High Density Coolant at Both Blowing Rates

Regions of near 80% reduction in effectiveness are distinguishable in the upstream near-hole region. The increased high-density coolant mass flux results in a nearly 120% increase in coolant momentum, facilitating jet lift-off from the endwall and leaving a largely uncooled region downstream of injection. Additional streaks of 20-40% film effectiveness reduction are present, particularly near PS (0.5 C_{ax}) at 0.25 – 0.5 $^{y}/_{P}$, for increased blowing condition. The adverse pressure gradient formed near pressure side, suppresses coolant re-attachment and effectiveness. This is unseen in the low blowing case due to the attachment further upstream, which eliminates the need for reattachment in this adverse pressure region. In the throat of the passage little percent change in η is observed. Overall, these results indicate that increasing coolant blowing rate at high coolant density adversely affects near-hole and passage onset performance, but better penetrates and cools the suction and pressure sides, specifically near trailing edge. Figure 16 utilizes pitchwise averaged η values to further illustrate the tradeoff.

<u>Endwall Heat Transfer:</u>

Similar to the investigation of coolant blowing rate on film cooling performance, endwall heat transfer will be analyzed using the percent augmentation of Nu and normalized NHFR. These parameters, as described by Equation 15 and Equation 16, illustrate the variation in endwall NHFR and Nu with increasing coolant blowing rate.

$$\mathrm{NHFR}_{\mathrm{Normalized}} = \frac{\mathrm{NHFR}_{\mathrm{HM}}}{\mathrm{NHFR}_{\mathrm{LM}}}$$

Equation 15. NHFR for High Coolant Blowing Rate Normalized by Low Coolant Blowing Rate (High Density Condition Only)

$$\mathrm{Nu}_{\mathrm{Augmentation,M}} = \frac{\mathrm{Nu}_{\mathrm{HM}} - \mathrm{Nu}_{\mathrm{LM}}}{\mathrm{Nu}_{\mathrm{LM}}} \times 100$$

Equation 16. Endwall Nusselt Number Augmentation Due to Increased High Density Coolant Blowing Rate

Figures 17 and 18 house results from Equations 15 and 16 respectively. The color bar schemes were reversed from one to the other with regards to these parameters for clarity and consistency. Principally, blue regions are indicative of cooler regions, which correspond to a reduction in $\mathrm{Nu}_{\mathrm{Augmentation,M}}$, and an increase in $\mathrm{NHFR}_{\mathrm{Normalized}}$. With consistence, the opposing red regions are indicative of hotter regions, corresponding to increased regions of $\mathrm{Nu}_{\mathrm{Augmentation,M}}$ and reduced $\mathrm{NHFR}_{\mathrm{Normalized}}$.

With an understanding of the color scheme and its implications, it is observed that the $\mathrm{Nu}_{\mathrm{Augmentation,M}}$ and $\mathrm{NHFR}_{\mathrm{Normalized}}$ look very similar in trend. This identifies that the primary mechanism for increasing endwall heat flux is increased Nu for the high blowing case. This is observed particularly in the upstream near-hole region and progressing to 0.5 C_{ax}. In general, the regions with large $\mathrm{Nu}_{\mathrm{Augmentation,M}}$ correspond to regions or decreased normalized NHFR. These regions of adverse thermal performance are attributed to the increased freestream turbulence imparted by the coolant jetting from the endwall, and the near pressure side adverse pressure gradient.

With progression into the passage, large pitchwise variances in both parameters are identified at 0.6 C_{ax}. At mid-pitch, a streak of near unity is present for normalized NHFR, and zero change Nu augmentation, indicating that in this small region, the effect of increasing high density coolant blowing rate is small. Conversely, large regions of $\mathrm{NHFR}_{\mathrm{Normalized}}$ increases and $\mathrm{Nu}_{\mathrm{Augmentation,M}}$ reduction are identified near pressure and suction sides and extending into and beyond the throat region. The more favorable heat transfer mechanisms distinguishable in these regions are attributed to the suppression of the PS and SS horseshoe vortex systems due to increased blowing. The counteraction of the HSV formation is evident by blue traces. These traces increase in size with progression through the passage, due to the growing size and intensity of both

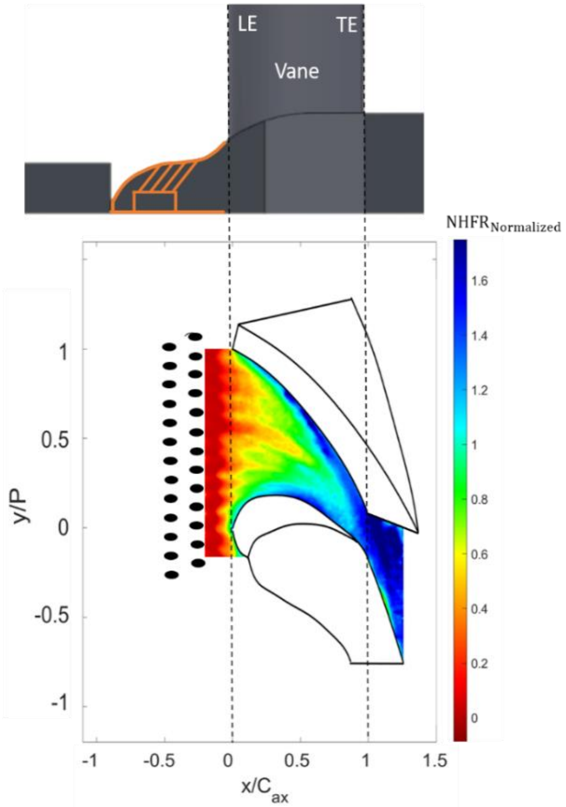

Figure 17. Normalized NHFR for Varied High Density Coolant Blowing Rate

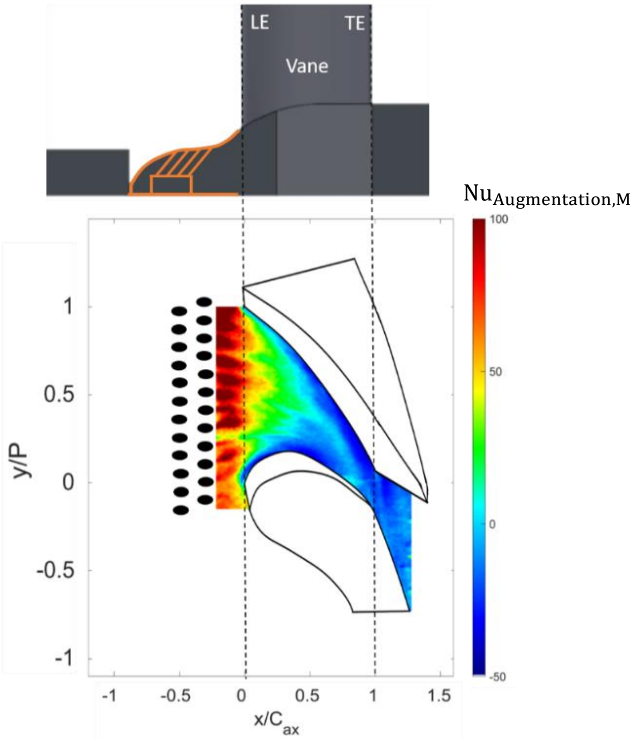

Figure 18. Nusselt Number Augmentation Due to Increased High Density Coolant Blowing Rate

horseshoe vortices when unsuppressed, as in the low blowing high density condition. The ability of the high density coolant at high blowing condition to suppress and shield these portions of the endwall grows through the passage, becoming very substantial in the throat. Overall, it is concluded that endwall heat transfer is largely affected by high density coolant blowing rate. Low blowing rates that facilitate better coolant attachment following hole decreased turbulence levels greatly, and the heat transfer mechanisms in the upstream region of the passage are improved. However, this is reversed in the downstream regions of the passage, where the high blowing rate allows for better secondary flow suppression and subsequent endwall shielding in passage.

Summary and Concluding Remarks

This investigation is the first known to study and provide the effects of coolant density and high density coolant blowing rate for a purge jet cooling scheme at engine representative mainstream and coolant conditions. The geometry and conditions used were typical of an industry standard nozzle guide vane platform. The data presented were gathered at the Virginia Tech Transonic Wind Tunnel using IR thermography and reduced using a combination of methods provided by Cook and Felderman [59] and Xue et al. [60]. Oil paint flow visualization was employed to understand the flow physics, and high fidelity endwall η, Nu, and NHFR contours were compared to understand the heat transfer and film performance effects. The conclusions of this work are summarized in short below:

1) Coolant density should be accounted for in platform cooling scheme design, experimentation, and simulation. The neglect of coolant to mainstream density ratio could lead to a misprediction of thermal profile and hotspot severity near hole and in passage, ultimately leading to greater risks of thermal failure.

2) At low coolant blowing rates, low density coolant underpredicts near hole coolant effectiveness and heat transfer mitigation, but over predicts in high secondary flow regions. This leads to hot spot formation, particularly at the pressure side trailing edge.

3) For high blowing rates, coolant density effects were minimal due to increasingly dominant coolant momentum effects, especially jet lift-off.

4) Increasing high density coolant blowing rate increased coolant effectiveness in high secondary flow regions near pressure and suction side, but severely decreased thermal performance at mid-passage, particularly near vane leading edge.

To build upon the work presented herein, the following suggests future investigations that could further aid in the understanding of purge jet cooling scheme design and analysis. To further aid in the understanding of the results obtained herein, high frequency pressure measurements in critical regions could allow further insight into the fluid flow mechanisms at play. Recently, the instrumentation community has made large strides in developing high frequency pressure transducers that are small enough to be embedded. Kang et al. [68] recently demonstrated this cutting edge technology using a shock tube testing apparatus. In addition, often there are endwall geometric features not modeled in this experiment, including but not limited to thermal gradient and manufacturing tolerance induced combustor-vane interface misalignments and slashface geometry with leakage. It is widely shown in literature that these features largely effect endwall secondary flow, however, effects of each in the midst of modeling high density coolant remains unstudied, especially for a purge jet cooling scheme. Any attempts to more closely match endwall geometry and cooling mechanisms will further help the understanding of this complex problem.

Acknowledgements

This work was completed under the sponsorship of industry sponsors Hongzhou Xu and Michael Fox of Solar Turbines Inc., and the academic guidance of Dr. Wing Ng, Chris C. Kraft Endowed Professor at Virginia Tech.

References

[1] Benaboud, A., and Rufer, A., 2016, “Gas Turbine: Optimization of Energy Production and High Efficiency by Using Power Electronics,” Procedia Eng., **138**, pp. 337–346.

[2] Papa, M., Srinivasan, V., and Goldstein, R. J., 2011, “Film Cooling Effect of Rotor-Stator Purge Flow on Endwall Heat/Mass Transfer,” J. Turbomach., **134**(4), pp. 041014-041014–8.

[3] Han, J.-C., Dutta, S., and Ekkad, S., 2012, Gas Turbine Heat Transfer and Cooling Technology, CRC Press, Boca Raton, Florida.

[4] Sieverding, C. H., 1985, “Recent Progress in the Understanding of Basic Aspects of Secondary Flows in Turbine Blade Passages,” J. Eng. Gas Turbines Power, **107**(2), pp. 248–257.

[5] Sharma, O. P., and Butler, T. L., 1987, “Predictions of Endwall Losses and Secondary Flows in Axial Flow Turbine Cascades,” J. Turbomach., **109**(2), pp. 229–236.

[6] Jílek, J., 1986, “An Experimental Investigation of the Three-Dimensional Flow Within Large Scale Turbine Cascades,” ASME Turbo Expo: Power and Land, Sea, and Air, ASME, Dusseldorf, West Germany, pp. 1–10.

[7] Goldstein, R. J., and Spores, R. A., 1988, “Turbulent Transport on the Endwall in the Region Between Adjacent Turbine Blades,” J. Heat Transfer, **110**(4a), pp. 862–869.

[8] Wang, H. P., Olson, S. J., Goldstein, R. J., and Eckert, E. R. G., 1997, “Flow Visualization in a Linear Turbine Cascade of High Performance Turbine Blades,” J. Turbomach., **119**(1), pp. 1–8.

[9] Graziani, R. A., Blair, M. F., Taylor, J. R., and Mayle, R. E., 1980, “An Experimental Study of Endwall and Airfoil Surface Heat Transfer in a Large Scale Turbine Blade Cascade,” J. Eng. Power, **102**(2), pp. 257–267.

[10] Boyle, M. T., and Hoose, K. V., 1989, “Endwall Heat Transfer in a Vane Cascade Passage and in a Curved Duct,” ASME Turbo Expo: Power and Land, Sea, and Air, ASME, Toronto, Ontario, Canada, pp. 1–8.

[11] Kang, M. B., and Thole, K. A., 1999, “Flowfield Measurements in the Endwall Region of a Stator Vane,” ASME, ASME, Indianapolis, Indiana, pp. 1–9.

[12] Boyle, R. J., and Russell, L. M., 1990, “Experimental Determination of Stator Endwall Heat Transfer,” J. Turbomach., **112**(3), pp. 547–558.

[13] Ames, F. E., Barbot, P. A., and Wang, C., 2003, “Effects of Aeroderivative Combustor Turbulence on Endwall Heat Transfer Distributions Acquired in a Linear Vane Cascade,” J. Turbomach., **125**(2), pp. 210–220.

[14] Radomsky, R. W., and Thole, K. A., 2002, “High Free-Steam Turbulence Effects on Endwall Heat Transfer for a Gas Turbine Stator Vane,” J. Turbomach., **122**(4), pp. 699–708.

[15] Schmidt, D. L., and Bogard, D. G., 1996, “Effects of Free-Stream Turbulence and Surface Roughness on Film Cooling,” ASME Turbo Expo: Power and Land, Sea, and Air, ASME, Birmingham, UK.

[16] Laveau, B., Abhari, R. S., Crawford, M. E., and Lutum, E., 2015, “High Resolution Heat Transfer Measurements on the Stator Endwall of an Axial Turbine,” J. Turbomach., **137**(4), pp. 041005-041005–10.

[17] Spencer, M. C., Lock, G. D., Jones, T. V., and Harvery, N. W., 1996, “Endwall Heat Transfer Measurements in an Annular Cascade of Nozzle Guide Vanes at Engine Representative Reynolds and Mach Numbers,” Int. J. Heat Fluid Flow, **17**(2), pp. 139–147.

[18] Hippensteele, S. A., and Russell, L. M., 1988, “High-Resolution Liquid-Crystal Heat-Transfer Measurements on the End Wall of a Turbine Passage With Variations in Reynolds Number,” 25th National Heat Transfer Conference, ASME, Houston, Texas, pp. 1–15.

[19] de la Rosa Blanco, E., Hodson, H. P., and Vázquez, R., 2005, “Effects of Upstream Platform Geometry on the Endwall Flows of a Turbine Cascade,” ASME Turbo Expo: Power and Land, Sea, and Air, Reno-Tahoe, Nevada, pp. 735–745.

[20] Colban, W. F., Thole, K. A., and Zess, G., 2003, “Combustor Turbine Interface Studies—Part 1: Endwall Effectiveness Measurements,” J. Turbomach., **125**, pp. 193–202.

[21] Colban, W. F., Lethander, A. T., Thole, K. A., and Zess, G., 2002, “Combustor Turbine Interface Studies - Part 2: Flow and Thermal Field Measurements,” ASME Turbo Expo: Power and Land, Sea, and Air, ASME, Amsterdam, The Netherlands, pp. 1003–1009.

[22] Piggush, J. D., and Simon, T. W., 2006, “Heat Transfer Measurements in a First-Stage Nozzle Cascade Having Endwall Contouring: Misalignment and Leakage Studies,” J. Turbomach., **129**(4), pp. 782–790.

[23] Mayo, D. E., Arisi, A., Ng, W. F., Li, Z., Li, J., Moon, H.-K., and Zhang, L., 2017, “Effect of Combustor-Turbine Platform Misalignment on the Aerodynamics and Heat Transfer of an Axisymmetric Converging Vane Endwall at Transonic Conditions,” ASME Turbo Expo: Power and Land, Sea, and Air, ASME, Charlotte, NC, pp. 1–11.

[24] Li, Z., Liu, L., Li, J., Sibold, R. A., Ng, W. F., Xu, H., and Fox, M., 2018, “Effects of Upstream Step Geometry on Axisymmetric Converging Vane Endwall Secondary Flow and Heat Transfer at Transonic Conditions,” J. Turbomach., **140**(12), pp. 121008-121008–14.

[25] Gustafson, R., Mahmood, G., and Acharya, S., 2007, “Aerodynamic Measurements in a Linear Turbine Blade Passage With Three-Dimensional Endwall Contouring,” ASME Turbo Expo: Power and Land, Sea, and Air, Montreal, Canada, pp. 855–865.

[26] Panchal, K. V., Abraham, S., Ekkad, S. V., Ng, W., Lohaus, A. S., and Crawford, M. E., 2012, “Effect of Endwall Contouring on a Transonic Turbine Blade Passage: Part 2 - Heat Transfer Performance,” ASME Turbo Expo: Power and Land, Sea, and Air, ASME, Copenhagen, Denmark, pp. 151–161.

[27] Thrift, A. A., Thole, K. A., and Hada, S., 2011, “Effects of an Axisymmetric Contoured Endwall on a Nozzle Guide Vane: Convective Heat Transfer Measurements,” J. Turbomach., **133**(4), pp. 041008-041008–10.

[28] Thrift, A. A., Thole, K. A., and Hada, S., 2011, “Effects of an Axisymmetric Contoured Endwall on a Nozzle Guide Vane: Adiabatic Effectiveness Measurements,” J. Turbomach., **133**(4), pp. 041007-041007–10.

[29] Shih, T. I.-P., Lin, Y.-L., and Simon, T. W., 2000, “Control of Secondary Flows in a Turbine Nozzle Guide Vane by Endwall Contouring,” ASME Turbo Expo: Power and Land, Sea, and Air, ASME, Munich, Germany, pp. 1–13.

[30] Dossena, V., Perdichizzi, A., and Savini, M., 1998, “The Influence of Endwall Contouring on the Performance of a Turbine Nozzle Guide Vane,” ASME Turbo Expo: Power and Land, Sea, and Air, ASME, Stockholm, Sweden, pp. 1–11.

[31] Okita, Y., and Nakamata, C., 2008, “Computational Predictions of Endwall Film Cooling for a Turbine Nozzle Vane with An Asymmetric Contoured Passage,” ASME Turbo Expo: Power and Land, Sea, and Air, ASME, Berlin, Germany, pp. 1–11.

[32] Dunn, M. G., 2001, “Convective Heat Transfer and Aerodynamics in Axial Flow Turbines,” ASME Turbo Expo: Power and Land, Sea, and Air, ASME, New Orleans, Louisiana.

[33] Chyu, M. K., 2001, “Heat Transfer near Turbine Nozzle Endwall,” Ann. N. Y. Acad. Sci., **934**, pp. 27–36.

[34] Simon, T. W., and Piggush, J. D., 2006, “Turbine Endwall Aerodynamics and Heat Transfer,” J. Propuls. Power, **22**(2), pp. 301–312.

[35] Bogard, D. G., and Thole, K. A., 2006, “Gas Turbine Film Cooling,” J. Propuls. Power, **22**(2), pp. 249–270.

[36] Bunker, R. S., 2006, "Gas Turbine Heat Transfer: Ten Remaining Hot Gas Path Challenges," J. Turbomach., **129**(2), pp. 193–201.

[37] Lynch, S. P., and Thole, K. A., 2008, "The Effect of Combustor-Turbine Interface Gap Leakage on the Endwall Heat Transfer for a Nozzle Guide Vane," J. Turbomach., **130**(4), pp. 041019-041019–10.

[38] Saxena, R., Alqefl, M. H., Liu, Z., Moon, H.-K., Zhang, L., and Simon, T. W., 2016, "Contoured Endwall Flow and Heat Transfer Experiments with Combustor Coolant and Gap Leakage Flows for a Turbine Nozzle Guide Vane," ASME Turbo Expo: Power and Land, Sea, and Air, ASME, Seoul, South Korea.

[39] Roy, A., Blot, D. M., Ekkad, S. V, Ng, W. F., Lohaus, A. S., and Crawford, M. E., 2013, "Effect of Upstream Purge Slot on a Transonic Turbine Blade Passage: Part 2 - Heat Transfer Performance," ASME Turbo Expo: Power and Land, Sea, and Air, ASME, San Antonio, Texas, pp. 1–11.

[40] Oke, R. A., Simon, T. W., Burd, S. W., and Vahlberg, R., 2000, "Measurements in a Turbine Cascade Over a Contoured Endwall: Discrete Hole Injection of Bleed Flow," ASME Turbo Expo: Power and Land, Sea, and Air, ASME, Munich, Germany.

[41] Zhang, L. J., and Jaiswal, R. S., 2002, "Turbine Nozzle Endwall Film Cooling Study Using Pressure-Sensitive Paint," J. Turbomach., **123**(4), pp. 730–738.

[42] Zhang, L., and Moon, H. K., 2003, "Turbine Nozzle Endwall Inlet Film Cooling: The Effect of a Back-Facing Step," ASME Turbo Expo: Power and Land, Sea, and Air, ASME, Atlanta, Georgia.

[43] Zhang, L., and Moon, H. K., 2004, "Turbine Nozzle Endwall Inlet Film Cooling: The Effect of a Back-Facing Step and Velocity Ratio," ASME International Mechanical Engineering Congress and Exposition, ASME, Anaheim, California.

[44] El-Gabry, L., Xu, H., Liu, K., Chang, J., and Fox, M., 2018, "Effect of Coolant Injection Angle on Nozzle Endwall Film Cooling: Experimental and Numerical Analysis in Linear Cascade," ASME Turbo Expo: Power and Land, Sea, and Air, ASME, Oslo, Norway.

[45] Pedersen, D. R., Eckert, E. R. G., and Goldstein, R. J., 1977, "Film Cooling With Large Density Differences Between the Mainstream and the Secondary Fluid Measured by the Heat-Mass Transfer Analogy," J. Heat Transfer, **99**(4), pp. 620–627.

[46] Baldauf, S., Schulz, A., and Wittig, S., 1999, "High-Resolution Measurements of Local Heat Transfer Coefficients From Discrete Hole Film Cooling," J. Turbomach., **123**(4), pp. 749–757.

[47] Baldauf, S., Schulz, A., and Wittig, S., 1999, "High-Resolution Measurements of Local Effectiveness From Discrete Hole Film Cooling," J. Turbomach., **123**(4), pp. 758–765.

[48] Johnson, B., Tian, W., Zhang, K., and Hu, H., 2014, "An Experimental Study of Density Ratio Effects on the Film Cooling Injection from Discrete Holes by Using PIV and PSP Techniques," Int. J. Heat Mass Transf., **76**, pp. 337–349.

[49] Narzary, D. P., Liu, K.-C., and Han, J.-C., 2012, "Influence of Coolant Density on Turbine Blade Platform Film-Cooling," J. Therm. Sci. Eng. Appl., **4**(2), pp. 02102-021002–10.

[50] Chen, P., Gao, H., Li, X., Ren, J., and Jiang, H., 2018, "Effects of Endwall 3D Contouring on Film Cooling Effectiveness of Cylindrical Hole Injections at Different Locations on Vane Endwall," ASME Turbo Expo: Power and Land, Sea, and Air, ASME, Oslo, Norway.

[51] Li, X., Ren, J., and Jiang, H., 2015, "Film Cooling Effectiveness Distribution of Cylindrical hole Injections at Different Locations on a Vane Endwall," Int. J. Heat Mass Transf., **90**, pp. 1–14.

[52] Nasir, S., Carullo, J. S., Ng, W.-F., Thole, K. A., Wu, H., Zhang, L. J., and Moon, H. K., 2009, "Effects of Large Scale High Freestream Turbulence and Exit Reynolds Number on Turbine Vane Heat Transfer in a Transonic Cascade," J. Turbomach., **131**(2), pp. 021021-021021–11.

[53] Arisi, A., Phillips, J., Ng, W. F., Xue, S., Moon, H. K., and Zhang, L., 2016, "An Experimental and Numerical Study on the Aerothermal Characteristics of a Ribbed Transonic Squealer-Tip Turbine Blade With Purge Flow," J. Turbomach., **138**(10), pp. 101007-101007–11.

[54] Carullo, J. S., Nasir, S., Cress, R. D., Ng, W. F., Thole, K. A., Zhang, L. J., and Moon, H. K., 2010, "The Effects of Freestream Turbulence, Turbulence Length Scale, and Exit Reynolds Number on Turbine Blade Heat Transfer in a Transonic Cascade," J. Turbomach., **133**(1), pp. 011030-011030–11.

[55] Holmberg, D. G., and Diller, T. E., 2004, "Simultaneous Heat Flux and Velocity Measurements in a Transonic Turbine Cascade," J. Turbomach., **127**(3), pp. 502–506.

[56] Roy, A., Blot, D. M., Ekkad, S. V., Ng, W. F., Lohaus, A. S., Crawford, M. E., and Abraham, S., 2018, "Thermal Management of a Transonic Turbine: Leakage Flow and Endwall Contouring Effects," J. Thermophys. Heat Transf., **32**(4), pp. 1031–1044.

[57] Nix, A. C., Smith, A. C., Diller, T. E., Ng, W. F., and Thole, K. A., 2002, "High Intensity, Large Length-Scale Freestream Turbulence Generation in a Transonic Cascade," ASME Turbo Expo, ASME, Amserdam, Netherlands, pp. 1–8.

[58] Teekaram, A. J. H., Forth, C. J. P., and Jones, T. V., 1989, “The Use of Foreign Gas to Simulate the Effects of Density Ratios in Film Cooling,” J. Turbomach., **111**(1), pp. 57–62.

[59] Cook, W. J., and Felderman, E. J., 1966, “Reduction of Data from Thin-Film Heat-Transfer Gauges: A Concise Numerical Technique,” AIAA J., **4**(3), pp. 561–562.

[60] Xue, S., Roy, A., Ng, W. F., and Ekkad, S. V., 2015, “A Novel Transient Technique to Determine Recovery Temperature, Heat Transfer Coefficient, and Film Cooling Effectiveness Simultaneously in a Transonic Turbine Cascade,” J. Therm. Sci. Eng. Appl., **7**(1), pp. 011016-011016–10.

[61] Lynch, S. P., and Thole, K. A., 2017, “Heat Transfer and Film Cooling on a Contoured Blade Endwall With Platform Gap Leakage,” J. Turbomach., **139**(5), pp. 051002-051002–10.

[62] Li, W., Lu, X., Li, X., Ren, J., and Jiang, H., 2019, “Wall thickness and injection direction effects on flat plate full-coverage film cooling arrays: Adiabatic film effectiveness and heat transfer coefficient,” Int. J. Therm. Sci., **136**, pp. 172–181.

[63] Sen, B., Schmidt, D. L., and Bogard, D. G., 2010, “Film Cooling With Compound Angle Holes: Heat Transfer,” J. Turbomach., **118**(4), pp. 800–806.

[64] Roy, A., Jain, S., Ekkad, S. V., Ng, W., Lohaus, A. S., Crawford, M. E., and Abraham, S., 2017, “Heat Transfer Performance of a Transonic Turbine Blade Passage in the Presence of Leakage Flow Through Upstream Slot and Mateface Gap With Endwall Contouring,” J. Turbomach., **139**(12), pp. 121006-121006–11.

[65] Mick, W. J., and Mayle, R. E., 1988, “Stagnation Film Cooling and Heat Transfer, Including Its Effect Within the Hole Pattern,” J. Turbomach., **110**(1), pp. 66–72.

[66] Moffat, R. J., 1988, “Describing the uncertainties in experimental results,” Exp. Therm. Fluid Sci., **1**(1), pp. 3–17.

[67] Kline, S. J., and McClintock, F. A., 1953, “Describing Uncertainties in Single Sample Experiments,” Mech. Eng., pp. 3–8.

[68] Kang, Y., Sibold, R., Homer, M., Gladwin, L., Claus, R., Ng, W., and Ruan, H., 2019, “Semiconductor Nano and Micro Membrane Based Pressure Sensors for Wide Bandwidth Measurements,” ASME Turbo Expo: Power and Land, Sea, and Air, ASME, ed., Phoenix, Arizona.

Appendix A: All Results Obtained

Film Cooling Effectiveness:

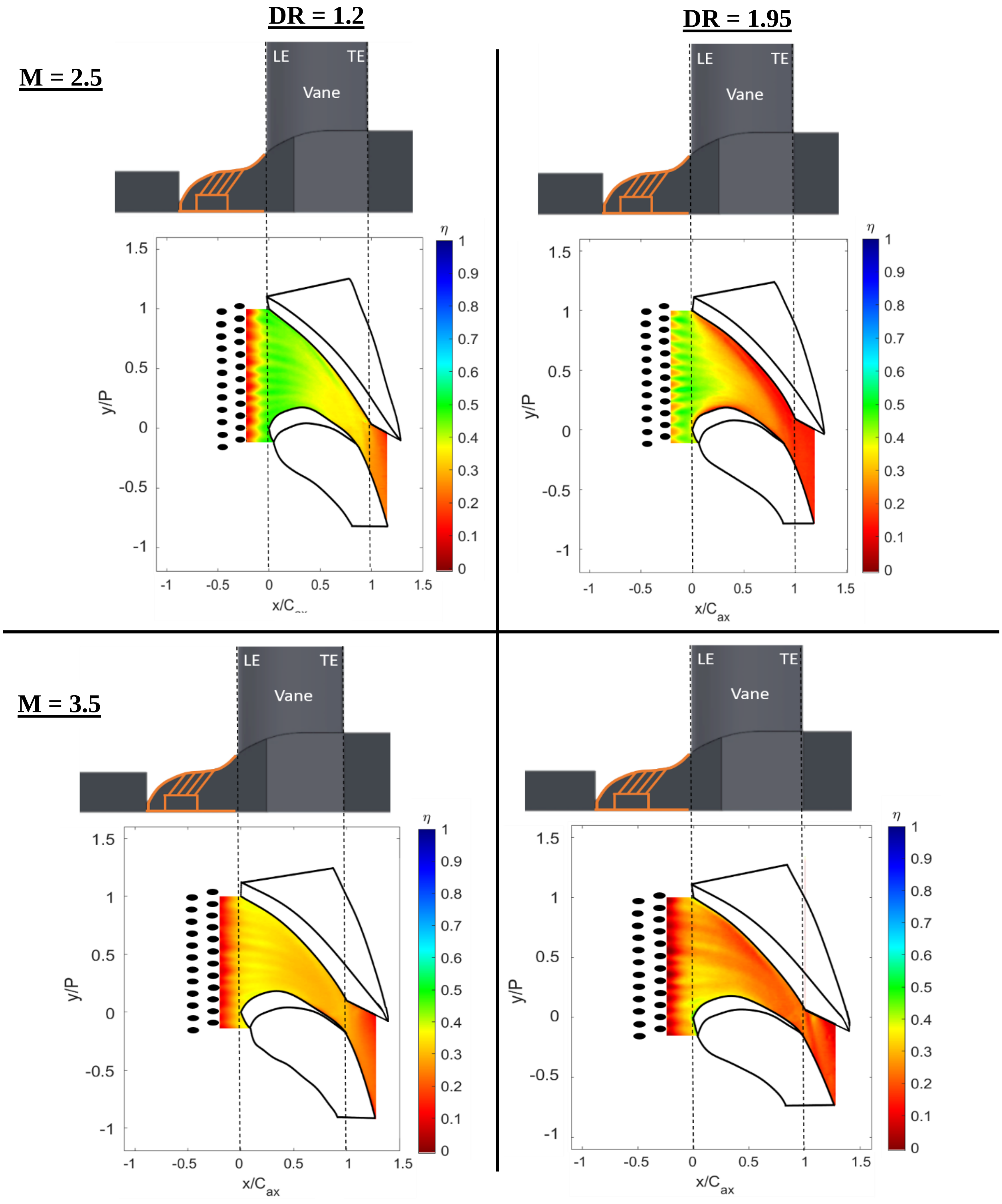

Figure 19. η Contours for All Test Cases

Nusselt Number:

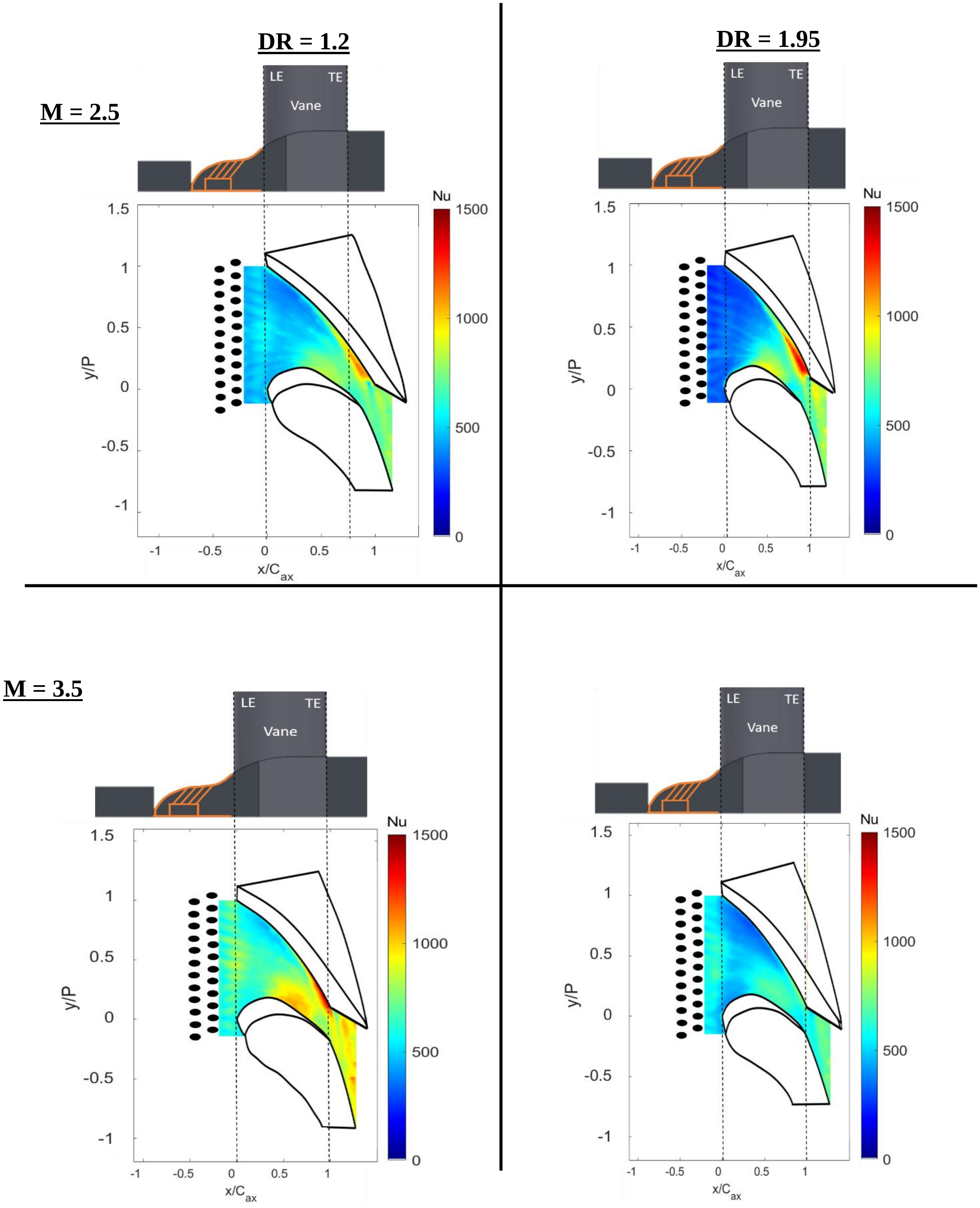

Figure 20. Nusselt Number Contours for All Test Cases

NHFR

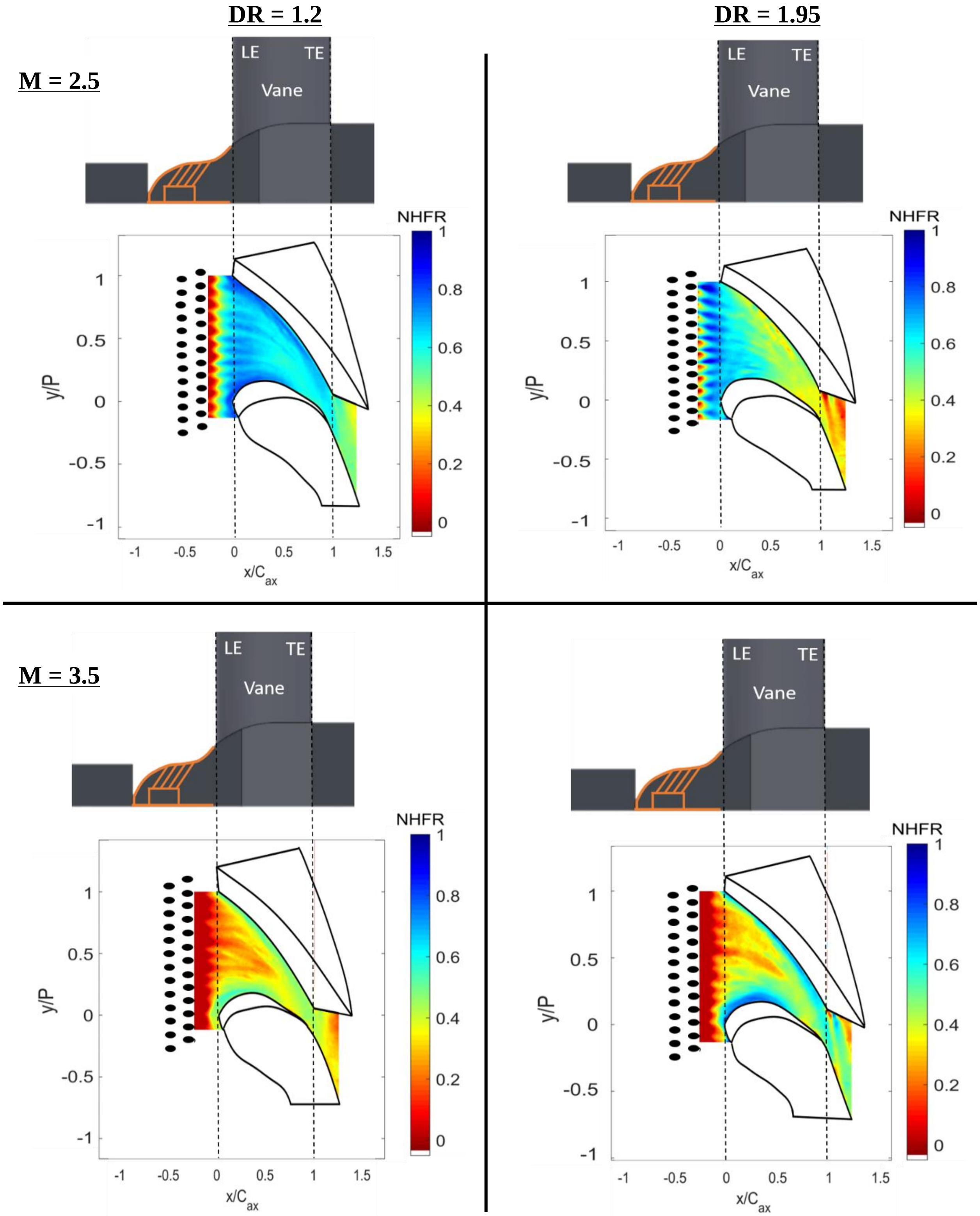

Figure 21. NHFR Contours for All Test Cases

Appendix B: Detailed Vane, Cooing Hole, and Endwall Geometry

The vane, cooling hole, and endwall geometry was given by industry sponsor Solar Turbines and scaled up 1.5x to obtain engine consistent exit Reynolds Numbers. For manufacturing purposes, the 4 vane linear cascade was split into 3 pieces with the top and bottom pieces containing one vane and the middle piece containing two. Each piece was 3D printed using an FDM method with a Stratasys Fortus 250mc. Following manufacturing, the pieces are mounted and sealed to a Lexan window using epoxy to ensure no leakage occured. For smoothness preservation, epoxy was sanded after drying. No leakage was ensured prior to each test run. Figure 22 shows a three-dimensional solid model of the manufactured vane pieces while mounted.

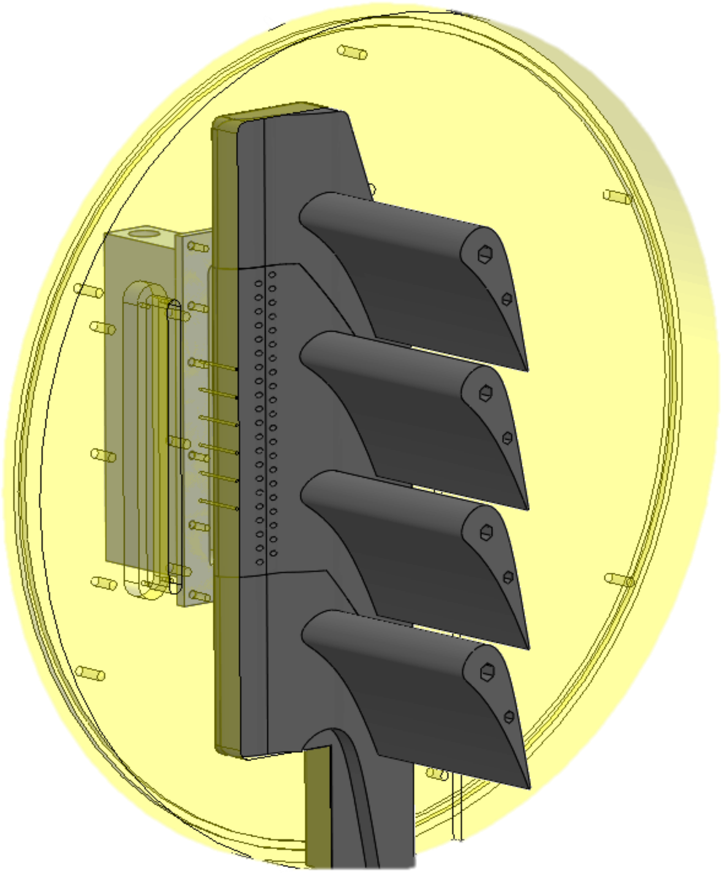

Figure 22. 3D Solid Model of 3 Piece Vane Cascade Mounted on Lexan Window

The axisymmetric vane endwall in this study was representative of an in-engine inner endwall profile. An upstream gap is apparent at 0.9 C_{ax} upstream of the leading edge, representative of the interface between nozzle guide vane platform and combustor linear. Downstream of the combustor/platform interface, a doublet staggered cylindrical hole purge jet cooling scheme is centered at 0.38 C_{ax} upstream of the vane leading edge. The staggered nature of the cooling scheme aids in uniform coverage in the pitchwise direction. To ensure in-hole roughness and diameter uniformity, metal tubing was cut and epoxied into each hole. To ensure cooling hole L/D was engine representative, a small rectangular plenum undercuts the holes. Figure 23 illustrates endwall geometry and gives a detailed view of the cooling holes and small plenum.

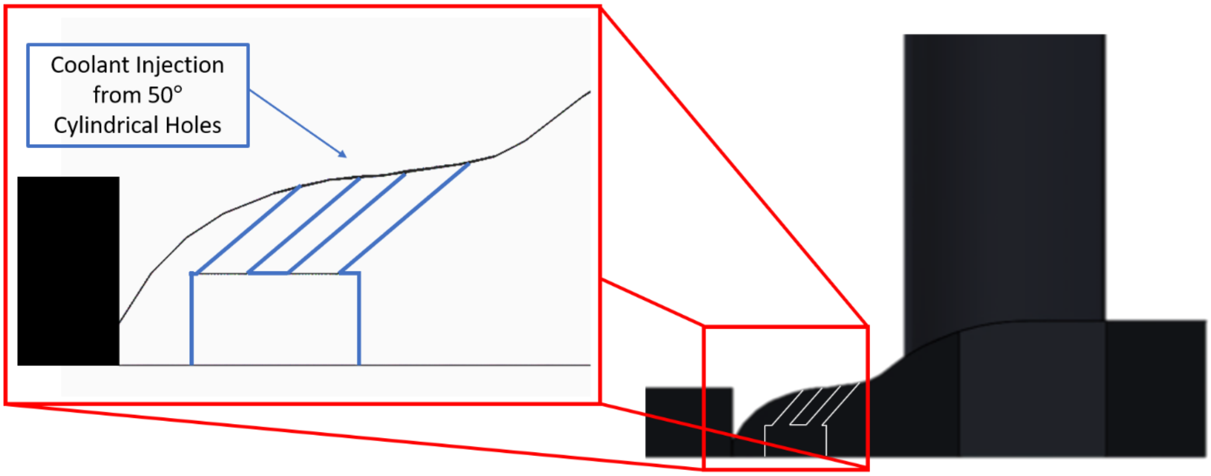

Figure 23. Pitchwise View of Endwall Geometry with Detailed Cutaway of Purge Jet Cooling Hole and Plenum Geometry

Appendix C: Mach Number Calculation for Mainstream Flow

For calculation of the inlet and exit Mach number a Pitot-Static probe and static pressure ports are employed. The Pitot-Static probe is located 2.8 $\mathrm{C_{ax}}$ upstream of the vane leading edge. Upstream and downstream static pressure ports are located at 1.4 $\mathrm{C_{ax}}$ upstream of the vane leading edge and downstream of the vane trailing edge respectively. For each region 6 equally pitchwise spaced ports are present. All pressure measurements are gathered and recorded using a NetScanner Model 98RK with an accuracy of $\pm$ 0.05% of the full scale. These pressures are then used to calculate the inlet and exit Mach number for the passage of interest according to Equation 17. The target exit Mach number for these tests was 0.85, which was matched with $\pm$5.0% error, as shown in Figure 24.

$$\mathrm{Ma} = \sqrt{\frac{2}{\gamma - 1}\left(\left(\frac{\mathrm{p_T}}{\mathrm{p_S}}\right)^{\frac{\gamma-1}{\gamma}} - 1\right)}$$

Equation 17. Mainstream Mach Number Calculation

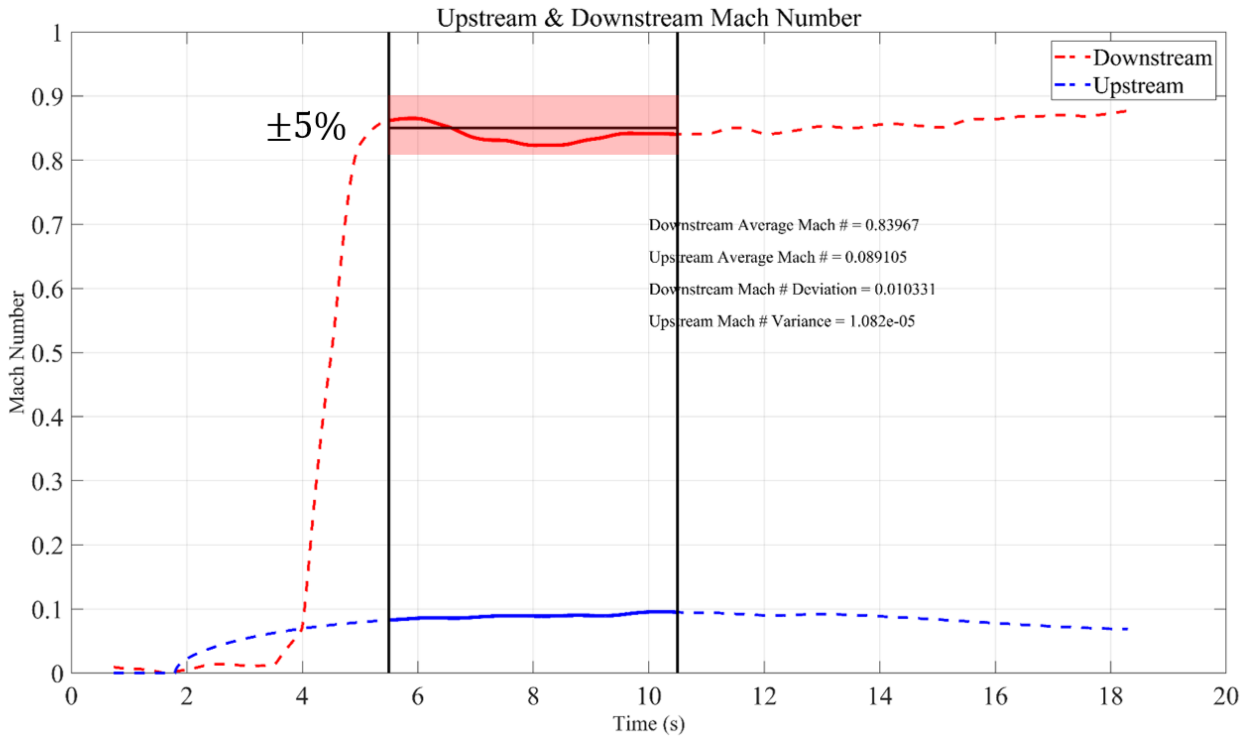

Figure 24. Example Mainstream Inlet and Exit Mach Number Plot with Highlighted Error Region

Appendix D: IR Surface Temperature Measurement

The passage of interest was tracked using a FLIR A325sc model infrared thermal camera. The data was acquired at a frequency of 30 Hz with an uncertainty to ± 2.0℃ or ± 2.0 % of the reading, whichever is greater. For viewing into the test section, a Germanium optical window was used due to superior thermal, mechanical, and optical properties. To further enhance the optical performance, a broad band anti-reflective coating was applied. The window was tested following fabrication by the manufacturer, Rocky Mountain Instrument Co., and found to have an average of 95% transmission in the wavelengths of interest (6 – 13 μm for the FLIR camera employed).

Prior to testing, the IR camera was tested, calibrated, and certified by FLIR. To investigate the effects of the Germanium window and contoured endwall, the camera was calibrated through the optical window at temperature ranges of $75 - 155$ °F. Small surface mount thermocouples were attached to the upstream and downstream regions of the flat black endwall to account for endwall contouring effects and compared with the IR reading. Figure 25 shows the calibration curve acquired. Results show that the camera is able to be linearly calibrated to account for the Germanium optical window and endwall contouring according to the equation shown. These results were applied to the gathered temperatures prior to data reduction.

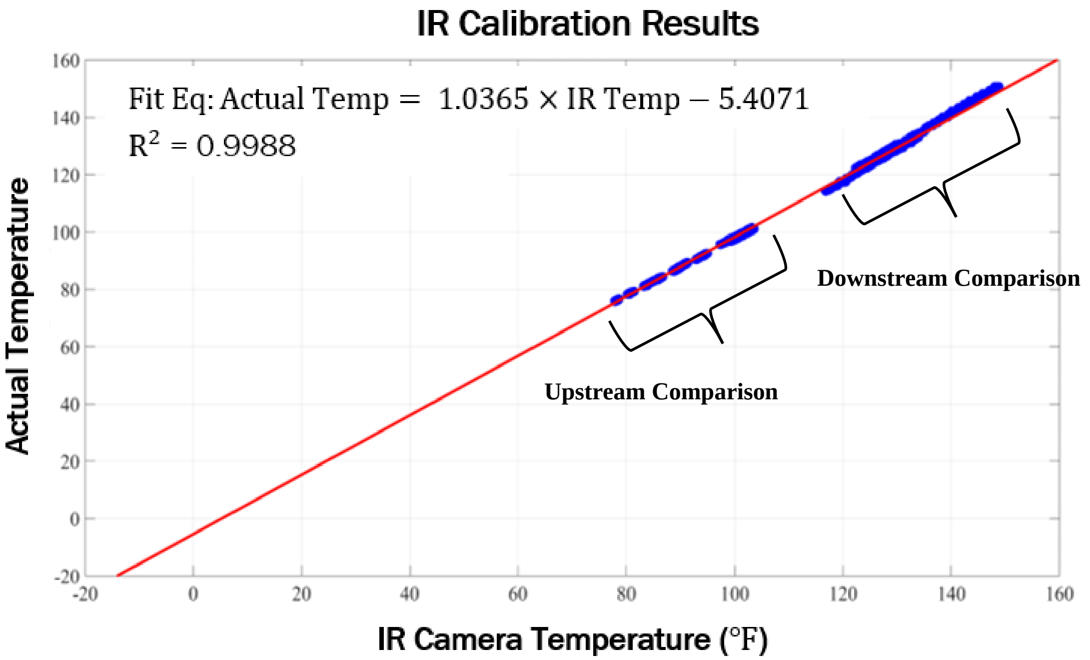

Figure 25. IR Camera Calibration Curve for Contoured Vane Endwall Through Germanium Optical Window

Appendix E: Purge Flow Coolant Delivery, Mixing, and Calculations

For this study, the blowing ratio, M, and density ratio, DR, were varied independently. For this, a two-coolant branch system was used to mix gases appropriately. One branch feeding the plenum was fed by a 100 gallon air tank pressurized to 120 psi. The second branch was fed by a Size 200 specialty gas cylinder housing pressurized industrial grade sulfur hexafluoride, SF_6. Teekaram et al. [58], amongst others has shown that foreign gases are a viable option for matching DR in heat transfer experiments. Figure 26 shows a detailed block diagram of the plumbing scheme with subsequent descriptions following.

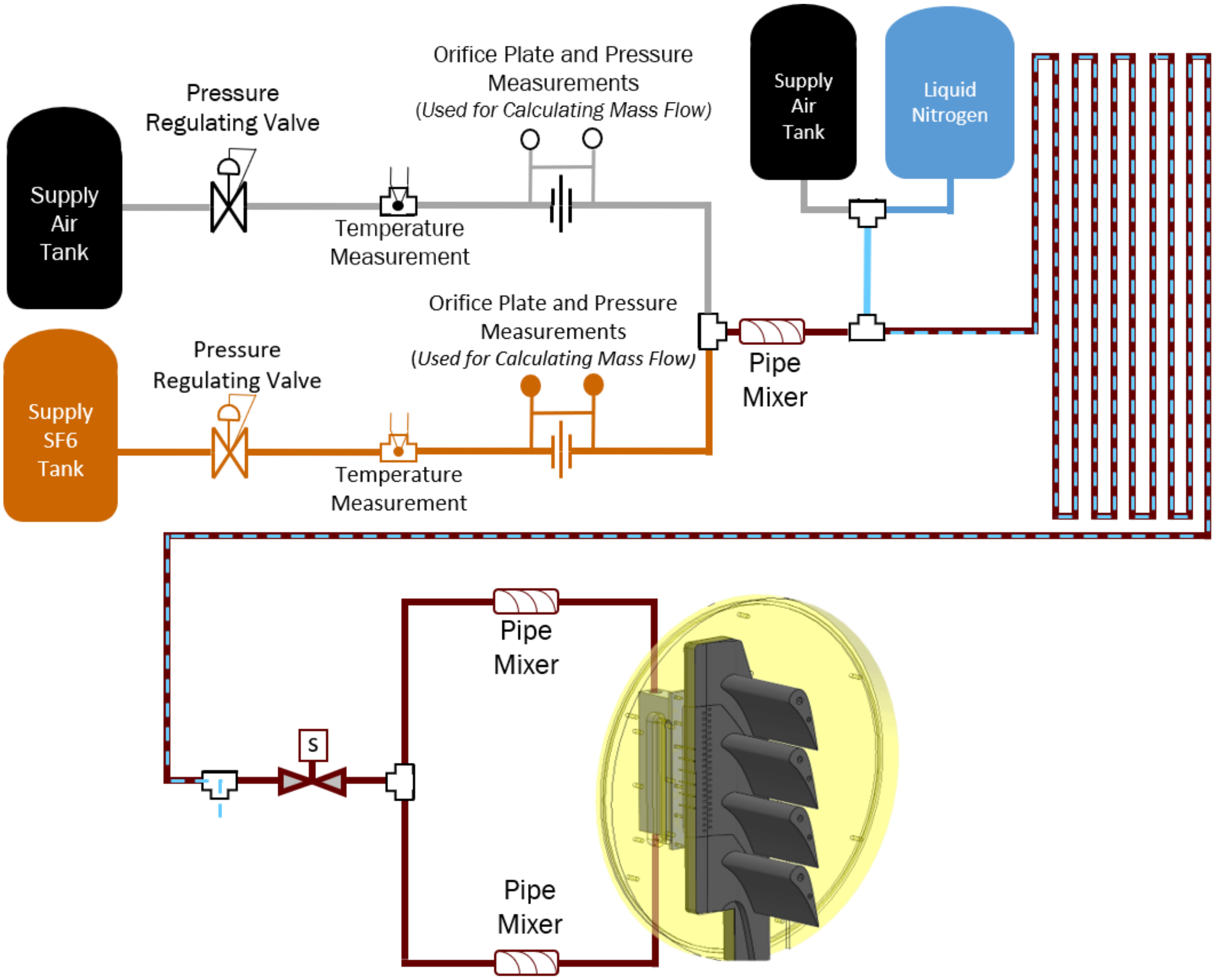

Figure 26. Detailed Purge Flow Plumbing Schematic

Each coolant branch was regulated by an upstream pressure regulator. The control of these upstream regulators allowed for the various coolant density and blowing rates to be achieved. The mass flow of each branch was independently measured using the combination of Lambda Square beveled and corner-tapped orifice plates, T-Type thermocouples, and pressure measurements upstream and downstream of the orifice. The measurements gathered in conjunction with Equation 18 allowed for a mass flow to be obtained, according to ISO 5167 Part B, for each branch. The Reader-Harris/Gallagher equation is used to calculate the coefficient of discharge from the orifice. Following, the industry standard equation for calculation of the expansibility factor was employed.

$$\dot{m} = C\epsilon A_2\sqrt{2\rho_1(p_1 - p_2)}$$

Equation 18. Mass Flow Calculation Through a Beveled and Corner Tapped Orifice Plate

<u>Where:</u>
$\dot{m}$ = mass flow through the orifice
C = coefficient of discharge
A_2 = cross sectional area of the orifice hole
ρ_1 = gas density upstream
p_1 = upstream pressure measurement
p_2 = downstream pressure measurement

Once the mass flow is properly calculated for each line, using conservation of mass, they can be summed to equal the mass flow in the complete system. From this, the blowing rate is calculated according to Equation 19. The blowing rate for each test case was held within an average deviation of ±3%, with a maximum deviation of 6%. Figure 27 shows an example plot of coolant blowing rate during tunnel blow down.

$$\left.\begin{array}{l} \mathrm{MFR} = \dfrac{\rho_c V_c A_c}{\rho_\infty V_\infty A_\infty} \\[2ex] M = \dfrac{\rho_c V_c}{\rho_\infty V_\infty} \end{array}\right\} \quad M = \frac{\rho_c V_c A_c A_\infty}{\rho_\infty V_\infty A_\infty A_c} \quad \Longrightarrow \quad \mathbf{M} = \frac{\dot{\mathbf{m}}_{\mathbf{c}} \mathbf{A}_\infty}{\dot{\mathbf{m}}_\infty \mathbf{A}_{\mathbf{c}}}$$

Equation 19. Blowing Ratio Calculation Formula

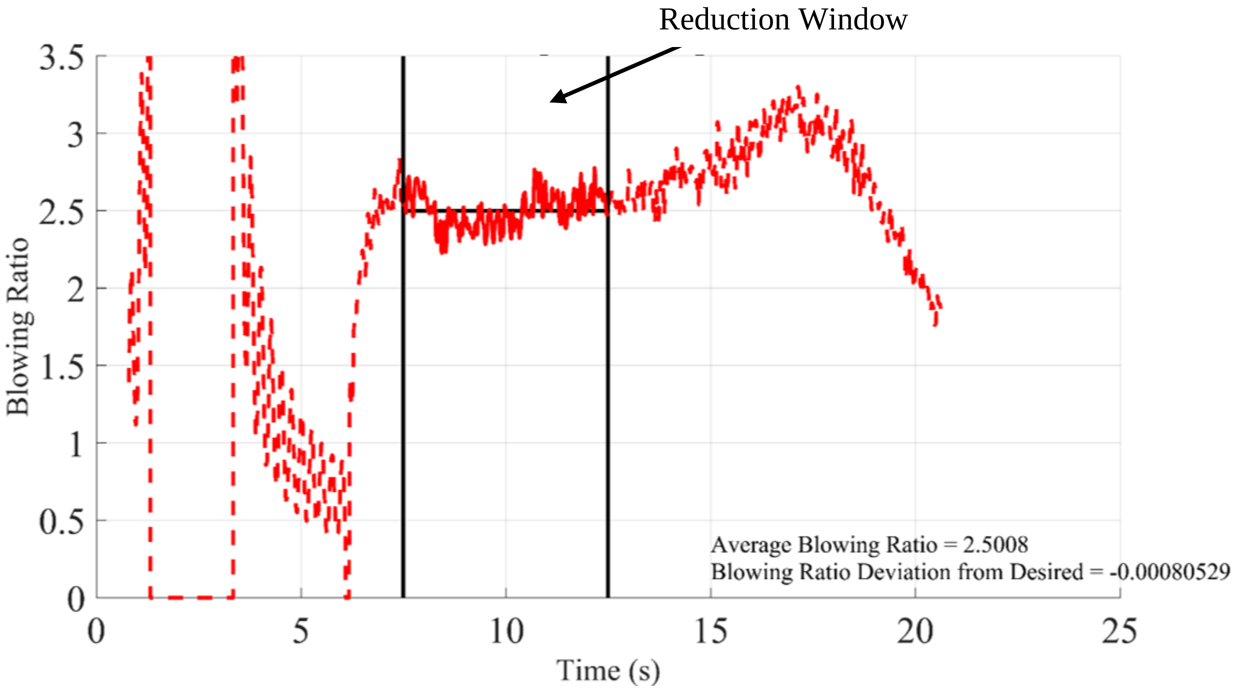

Figure 27. Example Blowing Ratio in Time Plot with Highlighted Reduction Window

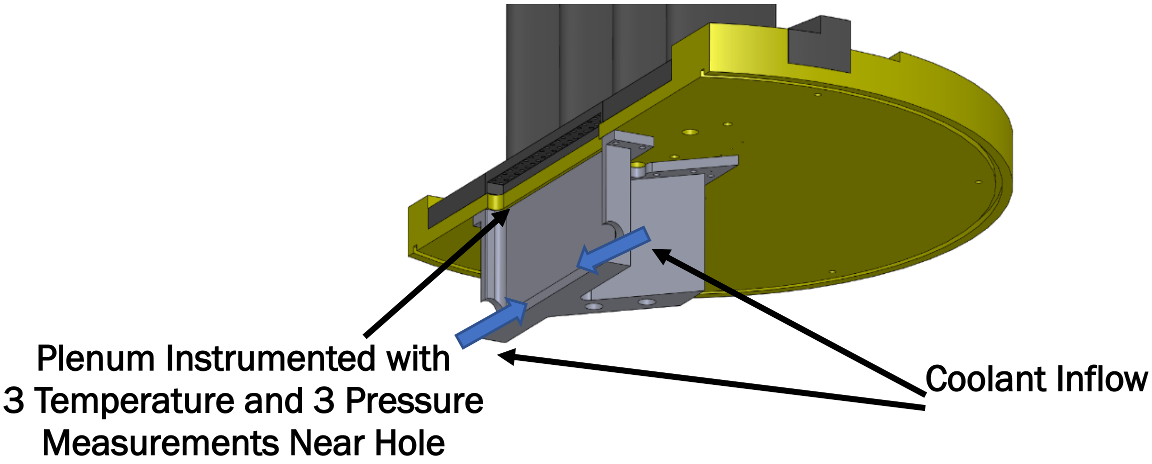

Figure 28. Plenum Cross Section

The coolant to mainstream density ratio reported was calculated based on the coolant conditions near hole entrance. For this, three temperature and pressure measurements were made in-plenum, as shown in Figure 28. Additionally, the specific gas constant for the mixture was calculated based on mass fractions of the constituents, calculated from the mass flow of each branch, in Equation 20. Figure 29 shows the result with an example coolant to mainstream density ratio plot as a function of time. Across all test cases the average deviation from ideal was ±3% with a maximum occurring at 6%.

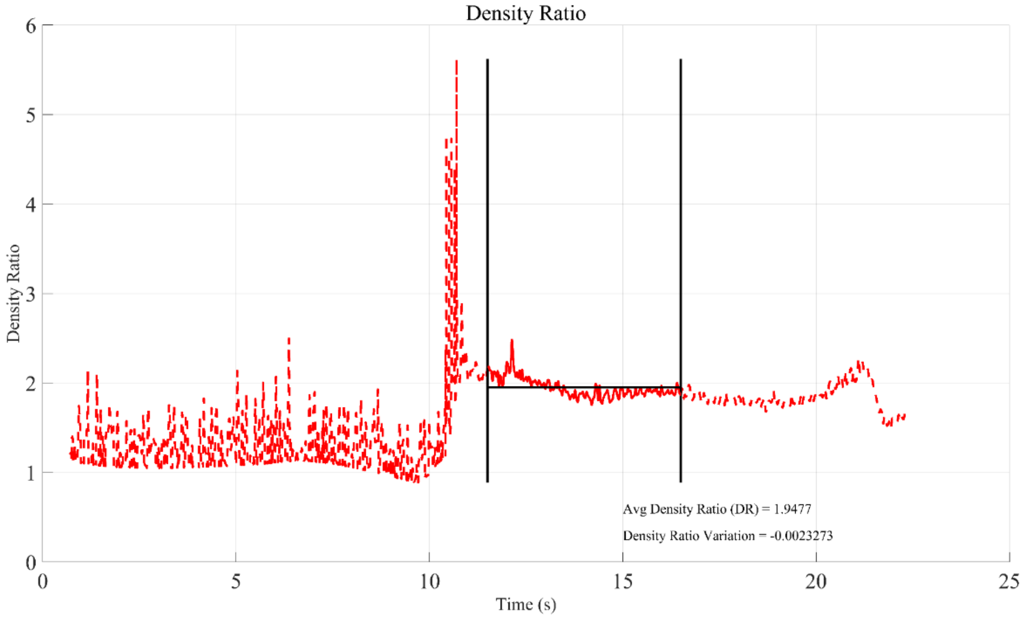

Figure 29. Example Coolant to Mainstream Density Ratio Plot as a Function of Time with Highlighted Reduction Region

Indicated by the blue line in Figure 26, a cooling loop was pre-chilled using an air and liquid nitrogen mixture. The mixture was pumped through the system and exhausted prior to the plenum, thus cooling the hosing and piping but avoiding precooling the endwall. This process was completed until the desired temperature was achieved. Following this, the test run ensued, with coolant flow controlled by a solenoid triggered by mainstream flow, and a transient coolant temperature profile was generated for the test run. Due to inherent advantages in the employed data reduction technique, the transience was of no concern. To ensure minimal gas stratification occurred, turbulent mixers were employed throughout.

Appendix F: Recovery Coefficient Determination for Dual Linear Regression

During the maximization process of the R^2 for the Dual Linear Regression Technique, criteria is set on Recovery Coefficient, $\mathrm{C_r}$, Recovery Temperature, T_r, Heat Transfer Coefficient, HTC, and Adiabatic Film Cooling Effectiveness, η. This in-house developed numerical method prevents convergence upon optimum R^2 values with unphysical results such as a Recovery coefficient or η values greater than 1 or less than 0, or an HTC less an 0. Figure 30 shows R^2, HTC, and η as a function of Recovery Coefficient with the solution marked.

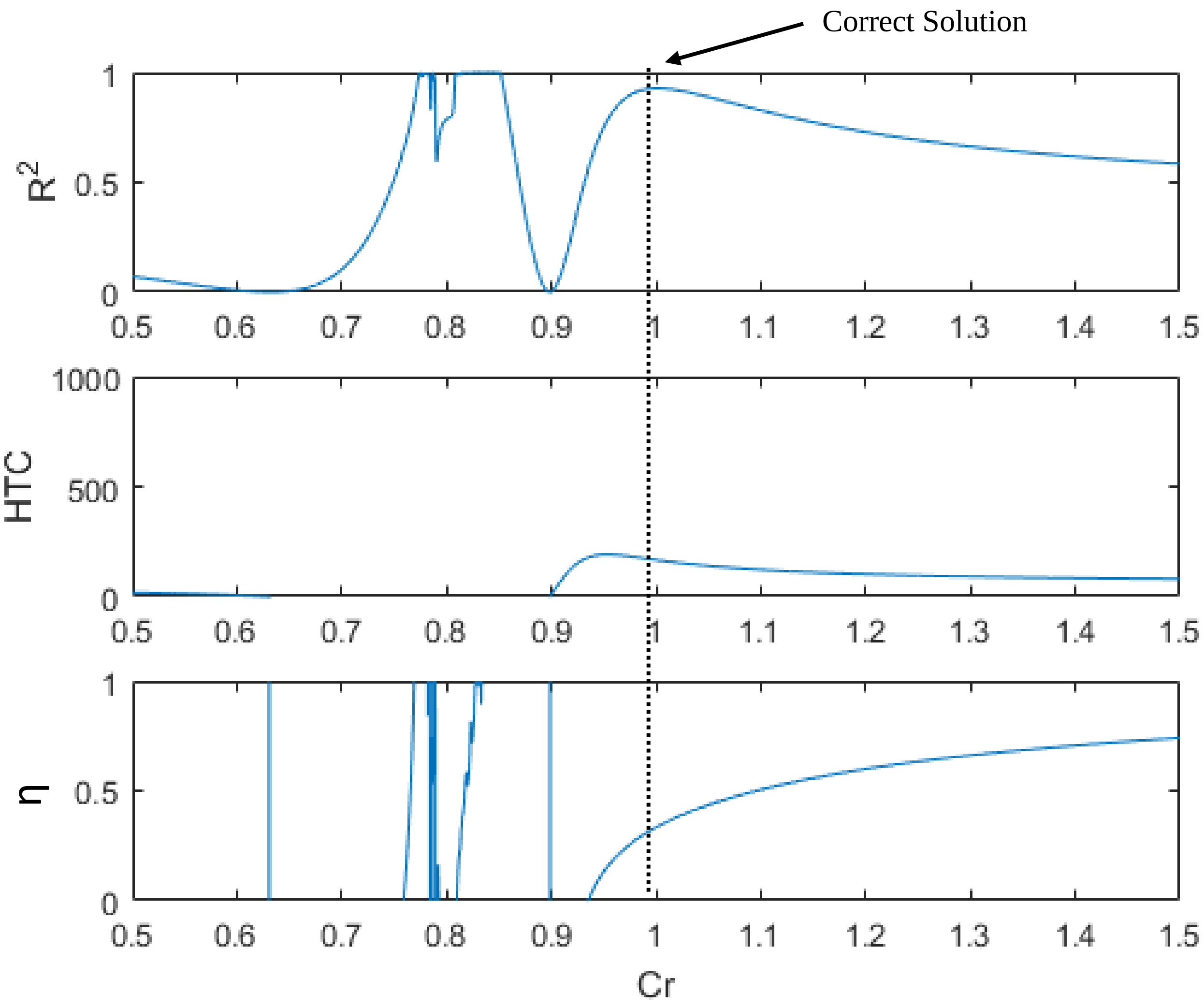

Figure 30. Example Recovery Coefficient Convergence During Dual Linear Regression for a Single Pixel